Eur. J. Mech. B/Fluids, **17**, n° 5, 689–737, 1998

Experimental and theoretical stability investigations of plane liquid jets

L. D. SÖDERBERG, P. H. ALFREDSSON *

ABSTRACT. – The present investigation has been undertaken in order to better understand the development of free, plane liquid jets. Both the development of the basic laminar flow as well as its stability have been investigated theoretically and experimentally.

The velocity field and free surface location of a liquid jet emanating from a plane channel was calculated numerically and the velocity and surface relaxation lengths were determined. Calculated velocity profile distributions were in good agreement with Pitot tube measurements.

Temporal linear stability calculations were performed using the calculated velocity distributions. The calculations showed five unstable modes, three sinuous and two dilatational. Four of these modes have been reported earlier and one of the sinuous modes is considered to be 'new'. The linear stability calculations include surface tension as well as viscosity in the liquid and gas.

Hot wire anemometry measurements of controlled forced disturbances showed that waves in the experimental jet also were sinuous and that the amplitude distribution was in fair agreement with theoretical results.

Shadowgraph visualisations showed the evolution of the waves on the surface of the jet and it was found that the waves break up downstream the nozzle. This break-up was visualized by particle visualisations, which showed that it creates strong streamwise streaks in the jet. © Elsevier, Paris

Keywords and phrases: – Jet, instability, transition, wave, visualization, shadowgraph, numerical calculation, break-up, hot-film anemometry.

1. Introduction

Plane liquid jets are used in several different industrial applications, and this study is aimed towards the paper industry, which, despite its long history, has not changed the basic principle of manufacturing. Paper making is still based on letting a suspension of water and fibres settle on a permeable surface which traps the fibres but allows the water to pass. As the water is removed the fibres form a network, a fibre mat, which after de-hydration becomes a paper sheet. Today the fibre suspension is formed into a plane liquid jet by a nozzle, a so called headbox, and distributed on one or between two moving permeable bands or wires. The velocity of the jet is 10-35 m/s and it is typically 5-10 m wide and 1 cm thick. The fibre suspensions which are fed to the paper machine usually have a fibre concentration less than 1% but still such a suspension is a non-Newtonian liquid where fibres tend to flocculate and form fibre networks.

The properties of a paper sheet are given by numerous parameters, e.g. quality of the pulp, forming method, chemical additives and so on. However, the conditions at the beginning of the forming process (inside the headbox and in the headbox jet), are believed to have a strong influence on the anisotropy and formation in the final paper sheet, *see i.e.* (Norman, 1996). Specifically streamwise oriented streaks in the jet are believed to be responsible for streaks in the final paper sheet.

Faxén Laboratory and Department of Mechanics, Royal Institute of Technology, S-100 44 Stockholm, Sweden
* Correspondence and reprints

0997-7546/98/05/© Elsevier, Paris

1.1. Previous studies of liquid jets

Free liquid jet flow has attracted much attention during the history of fluid mechanics and is used in many industrial applications, e.g. jet cutting, fuel injection and cooling through impingement. The research has historically been focused on the flow and break-up of cylindrical liquid jets in order to predict and control droplet size. For plane liquid jets research started in the middle of this century whereafter it gradually increased due to its industrial importance.

1.1.1. *Laminar flow of liquid jets*

If the flow of a plane jet is homogeneous in one direction it can be described as two-dimensional. Furthermore, if the jet is considered to be inviscid and irrotational (potential flow), a solution for the location of the free surface and the velocity field can be obtained by conformal mapping. The classical solution for a jet emanating from a two dimensional orifice (slit), can be found in many fluid dynamics textbooks, e.g. (Lamb, 1932), (Pai, 1954) or (Batchelor, 1967). This solution can be extended to a nozzle with varying angle of contraction, (Söderberg, 1994).

If the nozzle consists of an plane channel and the Reynolds number is low, the flow in the nozzle will be dominated by viscous forces. Given a sufficiently long channel this will result in the so called plane Poiseuille flow. The jet emanating from the channel will undergo a gradual relaxation from a fully developed parabolic profile to a uniform velocity distribution far downstream. This case was analysed theoretically by (Tillet, 1968) and the result is only valid for high Reynolds numbers, *see* (Joseph, 1978). Also, (Lienhard, 1968) solved the profile relaxation problem with an approximate method using the boundary layer equations.

(Nickell *et al.*, 1974) solved the flow of an incompressible viscous liquid jet at low Reynolds number $Re < 10^{-3}$ with the finite-element method. The aim was the die swell of a cylindrical Newtonian liquid jet, observed experimentally by (Middleman and Gavis, 1961).

The flow of a plane liquid jet emanating from a nozzle with varying contraction ratio, *i.e.* a converging nozzle, was investigated numerically by (Yu and Liu, 1992), also with the aim at the die swell phenomena. Their investigation covered Reynolds numbers within the range $0 < Re < 140$.

1.1.2. *Stability and break-up of cylindrical jets*

One of the earliest results concerning the hydrodynamics of liquid jets was obtained by (Plateau, 1873), who predicted the most probable droplet size by considering the surface area of a liquid cylinder based on the following consideration. Since surface tension can be expressed as a surface energy the minimisation of the surface area gives a surface energy minimum. For the liquid cylinder a minimum is obtained if the jet breaks up into pieces $2\pi a$ long, where a is the radius of the cylinder. Due to surface tension the pieces form drops after the break-up. The theoretical result was in agreement with experimental results by (Savart, 1833).

As one of the earliest results using linear stability theory, (Rayleigh, 1896) considered a liquid jet with a uniform velocity distribution, *i.e.* the flow is parallel and the velocity constant throughout the jet. Viscosity in the liquid was neglected, *i.e.* the flow was assumed to be inviscid and the effect of the ambient gas was neglected. Superficial forces were assumed to act on the surface of the jet and the analysis was performed by making an assumption of an infinitesimal perturbation acting on the surface of the jet. This gave as result a prediction of a growth or decay of the disturbances on the jet. The result showed that growth only could be obtained for axisymmetric disturbances with a wavelength λ that satisfies $\lambda > 2\pi a$, where a is the radius of the cylinder.

Later linear stability theory has been used extensively for various flow situations, *see* e.g. (Drazin and Reid, 1981). For the break-up of a cylindrical liquid jet the original approach by Rayleigh has been extended to include viscosity and non-linear effects. Investigations have been done both experimentally and numerically and is reviewed by (McCarthy and Molloy, 1974) and (Bogy, 1979). It has been shown experimentally, (Goedde

and Yuen, 1970), that non-linear effects cause ligaments between drops when the jet disintegrates. Also, it can be shown that the flow of a cylindrical liquid jet can be globally unstable, if proper boundary conditions are imposed at the upstream and downstream boundaries, (Yakubenko, 1997).

The effect of a non-uniform velocity distribution inside a cylindrical jet has also been considered, theoretically by (Leib and Goldstein, 1986) and experimentally by (Debler and Yu, 1988). The theoretical result was based on a spatial stability analysis and the conclusion is that the growth of a disturbance is reduced when the velocity profile in the liquid jet deviates from the uniform. The experiments by (Debler and Yu, 1988), were carried out by investigating the stability of a circular liquid jet emanating from tubes of varying length. With a constant flow rate through the tubes the profiles at the end of the tubes are more or less developed. The experiments gave qualitatively the same result as the theory, *i.e.* the growth rate is reduced with a non-uniform profile. The experiments also showed a significant effect of the upstream conditions on the break-up length of the jet. A higher turbulence level gave a more rapid disintegration of the jet. These investigations were all aimed at the break-up into discrete droplets by axisymmetric disturbances. This type of break-up is also denoted dilatational.

If the velocity of the jet is increased the break-up will be different, *see* (Hoyt and Taylor, 1977). They made visualisations of a circular liquid jet emanating from a converging nozzle which ended in a short straight pipe. The experiment also allowed for a co-flowing gas which could have a higher velocity than the liquid in the jet. Close to the exit short waves, *i.e.* their wavelength was much shorter than the jet diameter, could be seen. These waves were observed to break up a few jet diameters downstream the exit. The result of the break-up was formation of spray droplets, and the break-up was not sensitive to the velocity of the ambient gas. Further downstream a helical disturbance could be seen growing. This disturbance had a large amplitude and was enhanced by a higher velocity of the gas. The wavelength of the short waves were compared with linear stability results by (Brennen, 1970), which were obtained for a hydrodynamic cavity behind an axisymmetric body.

1.1.3. *Stability and break-up of plane liquid jets*

The stability of a plane liquid jet has not until recently been studied to the same extent as the cylindrical jet. A plane jet is basically two-dimensional with a thickness small compared to its width. Also, the basic flow is assumed to be symmetric with respect to the centreline of the jet. Due to the centreline symmetry a two-dimensional travelling wave disturbance can be either symmetric or anti-symmetric, *see* Figure 1.

Earlier work have studied the stability of plane liquid jets at different levels of approximation. If a liquid jet with no ambient gas is considered this can be done in basically the same manner and with the same assumptions of uniform velocity and surface tension as the study by (Rayleigh, 1896) of the circular jet, *see* (Drazin and Reid, 1981). This study shows that the jet is stable to all disturbances since surface tension always has a damping effect and forces the surface back to its rest state when perturbed. This is the opposite to the result for the circular geometry, since for the plane jet there is no transport of information from one surface of the jet to the other, hence energy minimum is obtained when the two surfaces are parallel.

To improve this result (Hagerty and Shea, 1955) included an ambient inviscid gas. This showed that the jet was unstable for both symmetric and anti-symmetric disturbances within a limited wavelength band. The origin

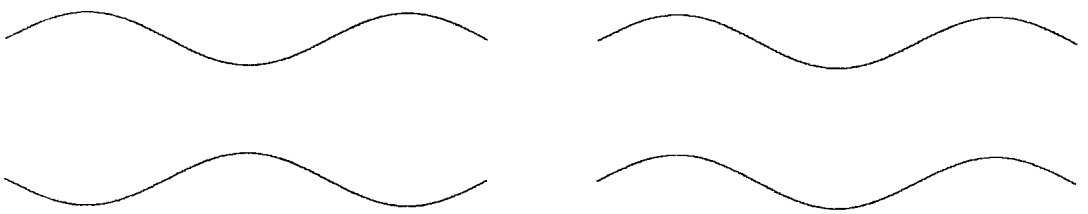

Fig. 1. – Definition of symmetry. Symmetric or dilatational (left) and antisymmetric or sinuous (right).

of this instability is the aerodynamic drag on the surface of the jet caused by the relative motion between the liquid and the ambient gas.

(Lin *et al.*, 1990) and (Li, 1991) improved this result by including viscosity in the liquid. The results from both of these investigations yield identical dispersion relations for the angular frequency and wavenumber.

$$\mathcal{F}(\alpha, \gamma, U, a, \nu_l, \rho_l, \rho_g) = 0,$$

where α is the wavenumber, γ the coefficient of surface tension, U the jet velocity, a the jet thickness, ν_l the kinematic viscosity of the liquid and $\rho_{l,g}$ the densities of the liquid and gas respectively. (Lin *et al.*, 1990) assumed that both the angular frequency and the wavenumber could be complex. This allows for both spatially and temporally growing disturbances. They found two convectively unstable modes, one symmetric and one anti-symmetric. Those are identical to the modes found by (Hagerty and Shea, 1955), but the growth rate is affected by the viscosity in the liquid. They also found an unstable even mode at zero frequency which was described as a pseudo-absolute instability. (Li and Tankin, 1991) also found the modes induced by the pressure fluctuation on the surface and showed the damping influence of viscosity. They also found that the even mode was enhanced by viscosity in a certain parameter range. These results, starting with (Hagerty and Shea, 1955) clearly showed that surface tension has a stabilising effect in contrast to the case for a cylindrical jet.

Recently (Teng *et al.*, 1997) included the effect of a viscous ambient gas bounded externally by solid walls. For this case viscosity in the gas has a damping effect. Also, (Luca and Costa, 1997), (Weinstein *et al.*, 1997) have studied the effect of spatial variation due to the presence of gravity on a vertically falling liquid sheet.

If the liquid jet emanates from a sufficiently long channel it will have a parabolic velocity distribution in the end of the channel. This profile will relax due to the change in boundary condition and somewhere downstream the velocity distribution will be uniform. This case was studied by (Hashimoto and Suzuki, 1991) experimentally and theoretically. By visualisations they found fine interfacial waves close to the nozzle which were explained by linear stability theory. A shooting method was used to solve the linear stability problem and this gave four unstable modes, two even and two odd. The first pair of these modes were called soft modes and the second pair were named hard modes. The hard modes had growth rates which were considerably higher when compared to the maximum growth rate for the first pair. The velocity profiles used in their stability calculations were taken from (Lienhard, 1968) and the effect of an ambient gas was not considered.

Experimental investigations concerning plane liquid jets have mainly been through flow visualisations, but also measurements of spray angle and break-up lengths have been made. (Mansour and Chigier, 1991) studied atomisation and investigated the break-up length of a plane liquid jet with co-flowing gas, where the gas has a higher velocity than the jet. This configuration is interesting since in combustion annular liquid jets with co-flowing high speed gas are used for fuel injection. Measurements of the turbulent flow field in a free liquid jet were made by (Wolf *et al.*, 1995).

1.2. Present work

The present work examines the flow and stability of a laminar plane liquid jet. A jet producing nozzle can have many different shapes, but to limit the investigation two canonical shapes of the nozzle have been considered, one which consists of a plane channel and the other which consists of a slit, Figure 2.

The channel nozzle is assumed to have a fully or partly developed laminar upstream flow. If the channel is long enough the velocity distribution in the channel will take the form of a parabola. When this emanates into an ambient gas with a lower viscosity and density the fluid inside the jet will be redistributed to eventually become uniform.

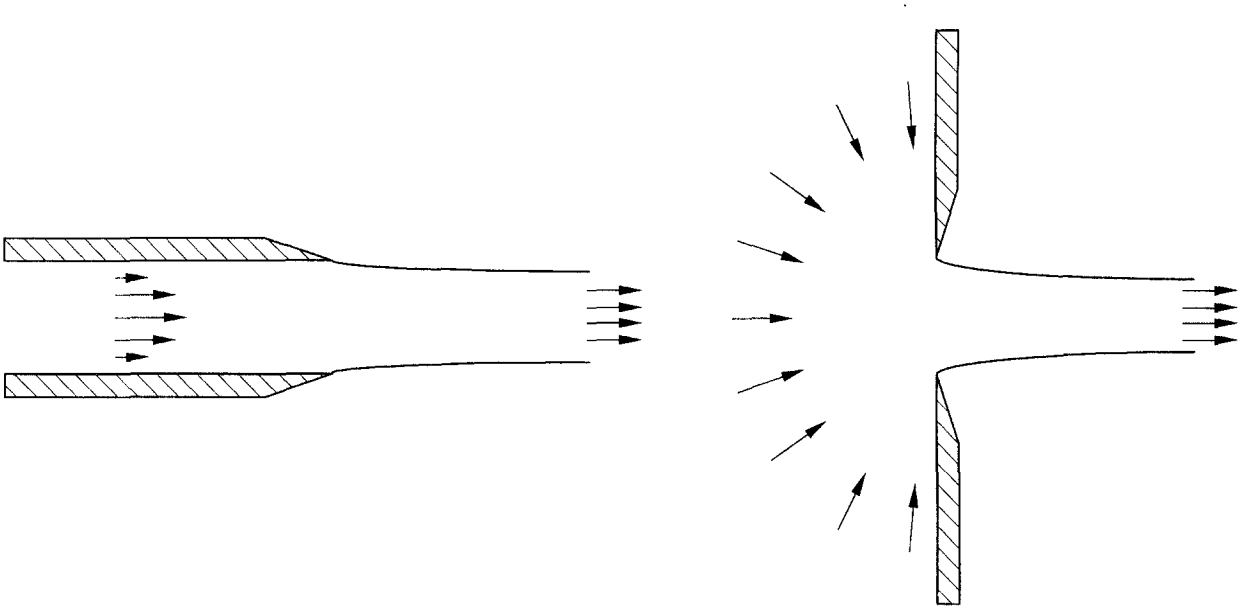

Fig. 2. – Nozzles used. Channel (left) and slit (right).

The process of velocity profile relaxation has been investigated numerically. The result is that the distance, ℓ_R, to reach a uniform velocity distribution is $\ell_R = 0.36aRe$, where Re is the Reynolds number based on half the channel height a and the mean velocity. This shows that the relaxation of the jet is a weaker process than for developing channel flow, for which the entrance length, ℓ_E, is given by $\ell_E = 0.16aRe$, *see* e.g. (Schlichting, 1979). Also, the calculation shows that this length is approximately independent of the flow profile at the nozzle outlet. The effect of a surrounding gas was also examined. If the viscosity of the gas is smaller than the viscosity of the liquid in the jet the effect was shown to be small. Experimental measurements of the velocity profile inside the jet was made with a Pitot tube. These were compared with calculations which showed a fair agreement confirming the theoretical calculations.

The flow through the slit nozzle on the other hand is mainly inviscid. It has been shown in numerical calculations that the location of the free surface, as predicted by inviscid theory, is in good agreement with numerical calculations and experiments for high contraction angles of the nozzle, *see* (Yu and Liu, 1992).

The instabilities of the jet flow were studied through flow visualisation using both the shadowgraph method and by adding reflective flakes to the water. Several different types of instabilities were observed. For the channel jet flow two-dimensional waves were observed on the surface of the jet. These waves grow in amplitude and break up. The particle visualisations show that the break-up occurs along a well defined line parallel to the nozzle. The break-up causes a streamwise streaky structure and a partial disintegration of the jet. This type of instability could not be found in the slit nozzle at any velocity possible to obtain in the experiments.

The jet emanating from the channel nozzle has been analysed with linear stability theory and five different unstable modes were found, three anti-symmetric and two symmetric. These are unstable for different wavenumbers and positions in the jet. In the experiments waves on the jet were triggered by acoustic excitation at velocities below where the 'natural' waves occurred. Measurements of these with the use of hot wire anemometry were performed, showing that the triggered waves were anti-symmetric. The spatial variation of the wavelength of the waves were obtained by image processing of the flow visualisation experiments.

2. Basic assumptions and geometry

A free liquid jet is produced by forcing a liquid through a nozzle and out into a gas. The characteristics of the jet depend on the geometry of the nozzle, upstream conditions and physical properties of the liquid and gas. Here the plane liquid jet is assumed to be emanating from a plane channel with an upstream specified flow. Both the liquid and gas are assumed to be incompressible Newtonian fluids, hence the equations governing the liquid and gas phases are the momentum equations

$$\frac{\partial u_i}{\partial t} + u_k \frac{\partial u_i}{\partial x_k} = -\frac{\partial p^{l,g}}{\partial x_i} + \frac{1}{Re^{l,g}} \frac{\partial^2 u_i}{\partial x_k \partial x_k} + \frac{1}{Fr^2} f_i, \quad i = 1, 2, 3. \tag{1}$$

and the continuity equation

$$\frac{\partial u_i}{\partial x_i} = 0, \tag{2}$$

where $\mathbf{u} = \mathbf{u}(\mathbf{x}, t) = u_i \mathbf{e}_i = u\mathbf{e}_x + v\mathbf{e}_y + w\mathbf{e}_z$, is the velocity vector, Re the Reynolds number, Fr the Froude number and f_i the i :th component of the unit vector in the direction of the gravitational acceleration. Superscripts l and g denote the liquid and gas phase respectively, a notation that will be used in the following.

Non-dimensionalisation has here been made with the half channel height, a, at the exit, $x = 0$, as the reference length scale and with the reference velocity defined from the flow rate Q through the nozzle, $U_m = Q/a$. This will give U_m as the mean velocity at the exit.

The Reynolds number, $Re^{l,g}$, and the Froude number, Fr, are hence defined as

$$Re^{l,g} = \rho^{l,g} U_m a / \mu^{l,g} \quad \text{and} \quad Fr = U_m / (ag)^{\frac{1}{2}},$$

where $\rho^{l,g}$ is the density, $\mu^{l,g}$ the dynamic viscosity and g the gravitational acceleration.

Since the Froude number is independent of density and viscosity it will be the same in the momentum equations for both phases. The relation between the Reynolds numbers in the two phases is

$$Re^g = \frac{\tilde{\rho}}{\tilde{\mu}} Re^l,$$

where $\tilde{\rho} = \rho^g / \rho^l$ is the density ratio and $\tilde{\mu} = \mu^g / \mu^l$ is the ratio of the dynamic viscosities. This also gives that

$$\tilde{p}^l = \tilde{\rho}\, \tilde{p}^g,$$

if the unscaled pressure p is the same in both liquid and gas.

The orientation and geometry of the nozzle can be seen in Figure 3, where the x-direction also will be referred to as the streamwise direction of the jet, the y-direction as normal and the z-direction, (not shown in the figure), as spanwise to the jet.

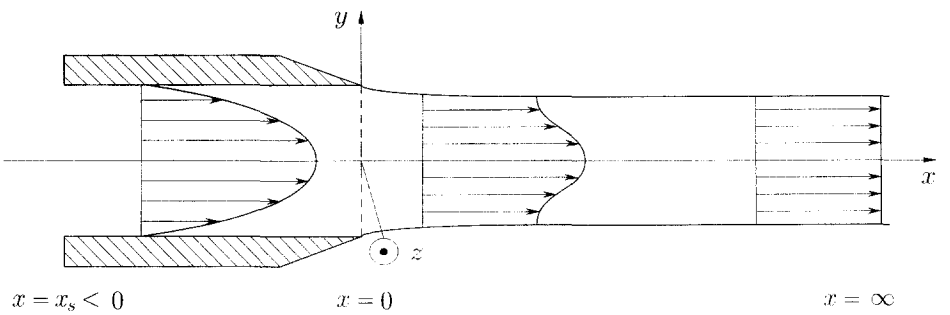

Fig. 3. – Principle of geometry and flow.

In (1) gravity is considered since in any type of experimental set-up or practical application gravity will always be present and either bend or stretch the jet depending on the direction to which it is directed. If the jet is directed in any other direction than vertical the stability of the jet will also be affected by gravity.

The gravity will only be taken into account to be able to compare experimental and numerical results, and when it is considered it is assumed to be acting only in the streamwise direction of the jet, which is consistent with the experimental set-up, ($\mathbf{f} = \{g, 0, 0\}$).

2.1. Boundary conditions

The equations describing the flow of the liquid jet and ambient gas as well as the location of the free surface have to be complemented with appropriate boundary and initial conditions. Inside the channel the walls consist of solid surfaces which give no-slip conditions for the flow,

$$u = v = w = 0 \quad \text{at} \quad y = \pm y_w, \quad x_s < x \leq 0.$$

For $x > 0$, *i.e.* for the free jet, boundary conditions must also be specified for the ambient gas away from the jet. Here all velocities are set to zero,

$$u = v = w = 0 \quad \text{at} \quad y = \pm\infty.$$

Also conditions that describe the liquid-gas interface have to be formulated. The liquid in the jet and the ambient gas is separated by a surface upon which surface tension forces acts, and the location of this free surface is given by

$$\mathcal{H}(x, y, z, t) = y - h(x, z, t) = 0. \tag{3}$$

where $h(x, z, t)$ is unknown. The location of the free surface is coupled to the velocity fields in the liquid by the kinematic condition that a liquid particle on the surface always will remain there. This gives that

$$\frac{\partial \mathcal{H}}{\partial t} + u_i \frac{\partial \mathcal{H}}{\partial x_i} = 0,$$

or by replacing $\mathcal{H}$ in this equation with the right hand side of (3),

$$\frac{\partial h}{\partial t} + u^{l,g} \frac{\partial h}{\partial x} + w^{l,g} \frac{\partial h}{\partial z} = v^{l,g} \quad \text{at} \quad y = h(x, z, t). \tag{4}$$

Hence the normal velocity of the surface is the same as the normal velocity v of a fluid element that exists there. This is true for the liquid in the jet as well as for the gas outside the jet.

If both phases are considered to be viscous there is a no-slip condition between the liquid and gas which gives that the velocities in all three directions have to be continuous across the free surface,

$$u_i^l = u_i^g \quad \text{at} \quad y = h(x, z, t), \tag{5}$$

which also implies continuous derivatives of any order of the primitive variables u_i or p, with respect to the streamwise or spanwise coordinates, x or z. This can be seen from

$$\frac{d}{dx} u_i^{l,g}(x, h) = \frac{\partial u_i^{l,g}}{\partial x} + \frac{dh}{dx} \frac{\partial u_i^{l,g}}{\partial h},$$

where the last term on the right hand side is identical for both phases. Hence

$$\frac{\partial u_i^l}{\partial x} = \frac{\partial u_i^g}{\partial x}, \tag{6}$$

which together with the continuity equation gives

$$\frac{\partial v^g}{\partial y} = \frac{\partial v^l}{\partial y}, \quad \text{at} \quad y = h(x, z, t). \tag{7}$$

The surface separating the liquid in the jet and the gas is subjected to pressure and viscous stresses from each of the phases, hence there has to be a force balance,

$$s_i^l - s_i^g = s_i^\gamma, \tag{8}$$

where $\mathbf{s} = s_i \mathbf{e}_i$ is the stress at the surface and γ denotes the superficial forces.

The stresses from the liquid and gas are given by projecting the stress tensor for each fluid phase,

$$\sigma_{ij}^{l,g} = -p^{l,g}\delta_{ij} + \frac{1}{Re^{l,g}}\left(\frac{\partial u_i^{l,g}}{\partial x_j} + \frac{\partial u_j^{l,g}}{\partial x_i}\right),$$

onto the normal of the surface, n_j,

$$s_i^{l,g} = \sigma_{ij}^{l,g} n_j \tag{9}$$

where the normal is given by

$$\mathbf{n} = \frac{\nabla \mathcal{H}}{|\nabla \mathcal{H}|} = \left(-\frac{\partial h}{\partial x}, 1, -\frac{\partial h}{\partial z}\right)|\nabla \mathcal{H}|^{-1}. \tag{10}$$

The surface is assumed to have an infinitesimal thickness and the jump in stress due to surface tension is a vector given by

$$s_i^\gamma = \frac{1}{We}\left(\frac{1}{R_x} + \frac{1}{R_z}\right)n_i = -\frac{1}{We}\frac{\partial n_j}{\partial x_j}n_i,$$

where We is the Weber number and R_x, R_z are the radii of curvature in the xy- and yz-planes respectively. The curvature, R_x, is here defined as positive for the case seen in Figure 4. The Weber number is here defined as

$$We = \rho^l U_m^2 a/\gamma,$$

where γ is the coefficient of surface tension. This gives three conditions at the surface, $i = 1, 2, 3$,

$$-(p^l - \tilde{\rho}p^g)\delta_{ij}n_j + \frac{1}{Re^l}\left(\frac{\partial u_i^l}{\partial x_j} + \frac{\partial u_j^l}{\partial x_i}\right)n_j - \tilde{\mu}\frac{1}{Re^l}\left(\frac{\partial u_i^g}{\partial x_j} + \frac{\partial u_j^g}{\partial x_i}\right)n_j = -\frac{1}{We}\frac{\partial n_j}{\partial x_j}n_i. \tag{11}$$

Because of the definition of the normal to the free surface, (10), these three conditions are all non-linear.

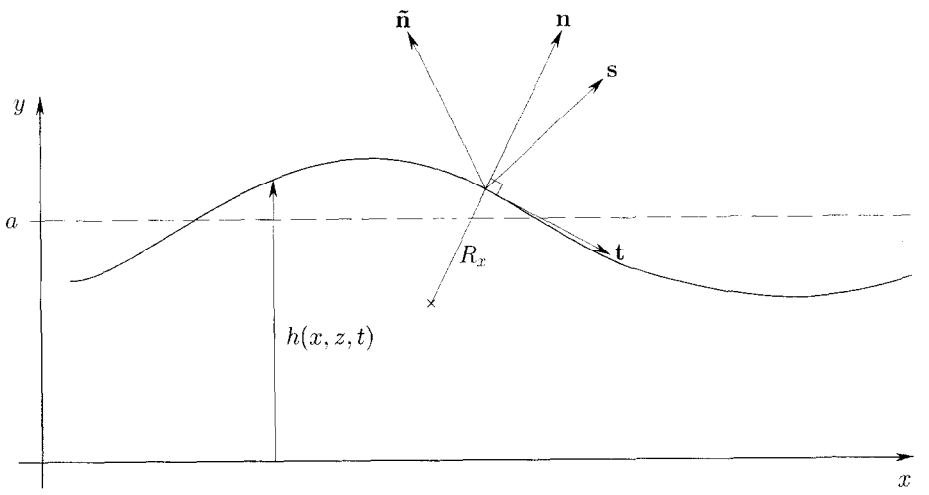

Fig. 4. – Definition of vectors on the free surface.

2.1.1. *Two-dimensional flow*

If the equations are restricted to a two-dimensional formulation in the xy-plane, the boundary conditions (11) can be reduced to

$$
\begin{aligned}
&-(p^l-\tilde{p}p^g)n_x+\frac{2}{Re^l}(1-\tilde{\mu})\frac{\partial u^l}{\partial x}n_x+\frac{1}{Re^l}\left(\frac{\partial u^l}{\partial y}-\tilde{\mu}\frac{\partial u^g}{\partial y}\right)n_y\\
&\quad+\frac{1}{Re^l}(1-\tilde{\mu})\frac{\partial v^l}{\partial x}n_y=-\frac{1}{We}\left(\frac{\partial n_x}{\partial x}+\frac{\partial n_y}{\partial y}\right)n_x,\\
&-(p^l-\tilde{p}p^g)n_y+\frac{2}{Re^l}(1-\tilde{\mu})\frac{\partial v^l}{\partial y}n_y+\frac{1}{Re^l}\left(\frac{\partial u^l}{\partial y}+\tilde{\mu}\frac{\partial u^g}{\partial y}\right)n_x\\
&\quad+\frac{1}{Re^l}(1-\tilde{\mu})\frac{\partial v^l}{\partial x}n_x=-\frac{1}{We}\left(\frac{\partial n_x}{\partial x}+\frac{\partial n_y}{\partial y}\right)n_y.
\end{aligned}
$$

where the conditions for continuous velocity at the surface have been used, (5)-(7). To simplify these the definition of the normal to the surface, (10), is used

$$
\begin{aligned}
&(p^l-\tilde{p}p^g)h_x-\frac{2}{Re^l}(1-\tilde{\mu})\frac{\partial u^l}{\partial x}h_x+\frac{1}{Re}\left(\frac{\partial u^l}{\partial y}-\tilde{\mu}\frac{\partial u^g}{\partial y}\right)\\
&\quad+\frac{1}{Re^l}(1-\tilde{\mu})\frac{\partial v^l}{\partial x}=-\frac{1}{We}\frac{}{dx}\left(\frac{h_x}{\sqrt{1+h_x^2}}\right)h_x,\\
&-(p^l-\tilde{p}p^g)+\frac{2}{Re}(1-\tilde{\mu})\frac{\partial v^l}{\partial y}-\frac{1}{Re^l}\left(\frac{\partial u^l}{\partial y}-\tilde{\mu}\frac{\partial u^g}{\partial y}\right)h_x\\
&\quad-\frac{1}{Re^l}(1-\tilde{\mu})\frac{\partial v^l}{\partial x}h_x=\frac{1}{We}\frac{d}{dx}\left(\frac{h_x}{\sqrt{1+h_x^2}}\right).
\end{aligned}
$$

The tangential shear on the surface is obtained if the stress, $\mathbf{s}$, is projected onto the tangent to the surface $\mathbf{t}=(n_y,-n_x)$,

$$\mathbf{t}\cdot(\mathbf{s}^l-\mathbf{s}^g-\mathbf{s}^\gamma)=0.$$

This gives

$$\frac{4}{Re^l}(1-\tilde{\mu})\frac{\partial v^l}{\partial y}h_x + \frac{1}{Re^l}\left(\frac{\partial u^l}{\partial y} - \tilde{\mu}\frac{\partial u^g}{\partial y}\right)(1-h_x^2) + \frac{1}{Re^l}(1-\tilde{\mu})\frac{\partial v^l}{\partial x}(1-h_x^2) = 0. \tag{12}$$

The stress, $\mathbf{s}$, can then be projected onto $\tilde{\mathbf{n}} = (n_x, -n_y)$, Figure 4,

$$\tilde{\mathbf{n}} \cdot (\mathbf{s}^l - \mathbf{s}^g - \mathbf{s}^\sigma) = 0,$$

which gives

$$-(p^l - \tilde{\rho}p^g)(1-h_x^2) + \frac{2}{Re^l}(1-\tilde{\mu})\frac{\partial v^l}{\partial y}(1+h_x^2) = \frac{1}{We}\frac{d}{dx}\left(\frac{h_x}{\sqrt{1+h_x^2}}\right)(1-h_x^2). \tag{13}$$

As can be seen from these boundary conditions, (12) and (13), the effect of a viscous ambient gas only enters through the pressure and the first normal derivative of the streamwise velocity.

The remaining boundary conditions are obtained from the assumption that the flow is symmetric with respect to the centreline of the channel and jet.

$$\frac{\partial u}{\partial y} = 0, \quad v = 0, \quad \frac{\partial p}{\partial y} = 0 \quad \text{at} \quad y = 0.$$

2.2. Flow of the surrounding gas

The flow of the surrounding gas depends on the geometry outside the jet. In order to investigate the effect of a viscous gas without making assumptions about the geometry and without having to solve the flow for the gas phase an approximate explicit expression for the tangential shear of the gas phase on the surface of the jet is assumed. This will give the unknown normal derivative of the streamwise velocity in the gas according to (12) and (13). The pressure is assumed to be constant in the gas.

To estimate the friction of the gas the solution to Stokes first problem, the infinite starting plate, *see* e.g. (Schlichting, 1979), is used,

$$u^g = u_{surface}(1 - \text{erf}\,\eta), \quad \text{where} \quad \eta = (y-a)/(\nu^g t)^{\frac{1}{2}}, \tag{14}$$

where $u_{surface}$ is the streamwise velocity of the surface of the jet. From this expression the tangential shear at the free surface in the streamwise direction is given by

$$\sigma = \mu^g \frac{\partial u^g}{\partial y} = -\mu^g u_{surface}(\pi\nu^g t)^{-\frac{1}{2}}, \tag{15}$$

where ν^g is the kinematic viscosity of the gas. The tangential shear is a function of time, t, but can be converted into a downstream distance by

$$t = U_m x.$$

With this substituted for t in (15) the shear at a position x of the surface is given by

$$\sigma = -\mu^g u_{surface}\left(\frac{U_m}{\pi\nu^g x}\right)^{\frac{1}{2}}.$$

This assumption for shear is considered only since an exact solution of the flow field in the gas outside of the jet depend on the far field conditions for the gas, and, when performing the stability analysis the analytical solution provides an easy access to the velocity distribution in the gas.

The explicit expression for the shear in the gas phase at the surface can be scaled to give,

$$\frac{\partial \tilde{u}}{\partial \tilde{y}} = -\tilde{u}_{surface}\left(\frac{U_m a}{\pi \nu^g}\frac{1}{\tilde{x}}\right)^{\frac{1}{2}} = -\tilde{u}_{surface}\left(\frac{Re^g}{\pi \tilde{x}}\right)^{\frac{1}{2}}.$$

2.3. Inlet and outlet conditions

Far upstream, *i.e.* $x \ll 0$, the flow enters a plane channel with a uniform velocity distribution. It then starts to develop and if the channel is long enough the result will be the well known case of plane Poiseuille flow. This developing flow has been described by (Schlichting, 1979) and gives the inlet length, ℓ_E, for fully developed Poiseuille flow as a linear function of Reynolds number,

$$\ell_E = 0.16 a Re$$

where Re is the Reynolds number based on half channel height a and mean velocity U_m. This expression is valid for high Reynolds, *see* (VanDyke, 1970).

3. Numerical solution of basic flow

The basic flow of a plane liquid jet is assumed to be independent of the spanwise coordinate z and therefore considered to be well described by the two-dimensional Navier-Stokes equations [1]. Further assumptions are that the flow is laminar, steady and symmetric with respect to the line given by $y = 0$.

To solve (1) and (2) numerically the method of finite differences has been used. A solution is sought in the domain bounded by

$$x_s \leq x \leq x_\infty,$$

in the streamwise direction, and

$$\begin{aligned} 0 \leq y \leq y_w \quad &\text{for} \quad x_s < x \leq 0, \\ 0 \leq y \leq h(x) \quad &\text{for} \quad 0 < x \leq x_\infty, \end{aligned}$$

in the normal direction. Here x_∞ is set to be a point far downstream of the nozzle where the flow is assumed to be parallel. The equations are solved for the primitive variables u, v and p. The domain is partly bounded by the free surface, which is unknown, and therefore the calculation has been made on an adaptive grid. This means that a new grid has to be generated everytime the location of the free surface changes in physical space. The surface will always coincide with a part of the top boundary in the computational domain, which will give a well defined surface as a part of the solution.

The transform which was used to map the physical domain onto the computational is given by

$$\xi = \xi(x, y) \quad \text{and} \quad \eta = \eta(x, y).$$

These variables represent a conformal transformation and satisfy the Laplace equation

$$\xi_{xx} + \xi_{yy} = 0 \quad \text{and} \quad \eta_{xx} + \eta_{yy} = 0.$$

[1] In the following all equations will be given in non-dimensional form, except where otherwise stated.

and the Cauchy-Riemann conditions

$$\xi_x = \eta_y \quad \text{and} \quad \xi_y = -\eta_x.$$

If these variables are introduced into (1) and (2), the following transformed equations are obtained

$$U^C \frac{\partial u}{\partial \xi} + V^C \frac{\partial u}{\partial \eta} = -\left(\frac{\xi_x}{J}\frac{\partial p}{\partial \xi} + \frac{\eta_x}{J}\frac{\partial p}{\partial \eta}\right) + \frac{1}{Re}\left(\frac{\partial^2 u}{\partial \xi^2} + \frac{\partial^2 u}{\partial \eta^2}\right), \tag{16}$$

$$U^C \frac{\partial v}{\partial \xi} + V^C \frac{\partial v}{\partial \eta} = -\left(\frac{\xi_y}{J}\frac{\partial p}{\partial \xi} + \frac{\eta_y}{J}\frac{\partial p}{\partial \eta}\right) + \frac{1}{Re}\left(\frac{\partial^2 v}{\partial \xi^2} + \frac{\partial^2 v}{\partial \eta^2}\right), \tag{17}$$

$$\frac{\partial U^C}{\partial \xi} + \frac{\partial V^C}{\partial \eta} = 0, \tag{18}$$

where the assumption of a steady flow has been used. Here J is the determinant of the Jacobian matrix, $\mathbf{J}$, of the transformation,

$$\mathbf{J} = \begin{bmatrix} \xi_x & \eta_x \\ \xi_y & \eta_y \end{bmatrix} \quad \Rightarrow \quad J = |\mathbf{J}| = \xi_x \eta_y - \xi_y \eta_x.$$

U^C and V^C are velocities in the transformed coordinate system in the ξ and η directions, respectively, given by

$$U^C = (\xi_x u + \xi_y v)/J \quad \text{and} \quad V^C = (\eta_x u + \eta_y v)/J.$$

A conformal transformation is by definition also orthogonal and has several advantages compared to a non-conformal transformation. The grid related parameters are limited and second derivatives of the transform variables, ξ and η, are not present in the equations. These may otherwise degrade the accuracy of the solution if the grid is distorted. The transform coordinates can also be interpreted as representing the potential and streamfunction of an inviscid irrotational flow in the geometry prescribed by the walls, centreline and free surface.

An adaptive conformal grid requires the Laplace equation for the transform variables to be solved repeatedly. The flow of the ambient gas was not calculated but instead treated explicitly by the approximation introduced in section 2.2.

3.1. Boundary conditions

In order to solve the transformed equations the boundary conditions has to be transformed too. The no-slip conditions at the wall (2.1), will not be affected by this,

$$u = v = 0 \quad \text{at} \quad y = y_w.$$

At the centreline the x and ξ coordinates are parallel, *i.e.* $\xi_y = 0$, and we obtain

$$\frac{\partial p}{\partial y} = \xi_y \frac{\partial p}{\partial \xi} + \eta_y \frac{\partial p}{\partial \eta} = \eta_y \frac{\partial p}{\partial \eta},$$

which is also true for the streamwise velocity u. Hence

$$\frac{\partial u}{\partial \eta} = 0, \quad v = 0, \quad \text{and} \quad \frac{\partial p}{\partial \eta} = 0 \quad \text{at} \quad \eta = 0. \tag{19}$$

The conditions for the stresses at the surface (11), contain several derivatives of the transformation variables. The expressions become complicated and are implemented as is. The velocity normal to the surface is parallel to the η direction in the computational domain which gives

$$V^C = 0 \quad \text{at} \quad \eta = 1. \tag{20}$$

This can be set in a more useful form with the aid of the transformed continuity equation, *see* (18), which can be integrated in the η direction. Together with (20) this results in an integral expression,

$$\int_0^1 \left(\frac{\partial U^C}{\partial \xi} + \frac{\partial V^C}{\partial \eta} \right) d\eta = \int_0^1 \frac{\partial U^C}{\partial \xi}\, d\eta + V^C|_{\eta=1} - V^C|_{\eta=0} = \frac{\partial}{\partial \xi} \int_0^1 U^C\, d\eta = 0$$

$$\Rightarrow \quad \int_0^1 U^C\, d\eta = \text{constant}.$$

This replaces the kinematic condition at the free surface. Totally there are six conditions. Five of these are needed to solve the equations of motion and one to find the location of the free surface.

3.2. Discretisation and solution method

The equations (16)-(18), are discretised by the method of finite differences. The computational domain is rectangular and the grid equidistant. The dependent variables u, v and p are evaluated at the same point. Since the conformal transformation gives the potential flow in the geometry prescribed by the wall, centreline and free surface, the viscous and inviscid flowfields are assumed to be similar, if the streamfunction is considered. Hence the flow will be close to parallel in the computational domain. All second derivatives are represented with central differences and the first order derivatives by a mixed upwind-central difference scheme

The discretised equations (16)-(18), are solved by an iterative method. First the initial grid is calculated. This is done by using the location of the free surface given by the solution to the flow of a potential jet. The initial guess for the flow is also taken from this solution. Starting with this initial guess the equations are solved implicitly in the η-direction starting at the upstream boundary, $j = 3$. The first two ξ positions are determined by the choice of inlet conditions. If, for example, a plane channel with fully developed flow is investigated, the velocity distribution in the η-direction is the same for both points, which is equal to setting $v = 0$ as a boundary condition. At the centreline, the boundary conditions (19) are specified at all streamwise positions, whereas inside the nozzle no-slip velocity conditions are used at the wall. When the equations are solved for the flow in the jet conditions (20) and (12) are used instead of the no-slip conditions.

The flow is solved iteratively with subsequent downstream marches and underrelaxation. During these iterations the free surface is fixed and when the solution is sufficiently converged the location of the surface is corrected with the aid of the remaining boundary condition (4). After correcting the location of the surface the Laplace equations for the transform variables are solved and derivatives of the transform variables re-evaluated. This iterative procedure is repeated until the solution is sufficiently converged.

3.3. Results for the basic flow

Calculations have been performed with the primary aim to provide basic velocity distributions for stability calculations but also to give some insight in the laminar flow of plane liquid jets. The liquid jet is initially assumed to be emanating into vacuum from a plane channel with an upstream parabolic velocity distribution, *i.e.* plane Poiseuille flow, but calculations were also made to study effects of a partly developed flow, a viscous ambient gas and gravity acting in the streamwise direction.

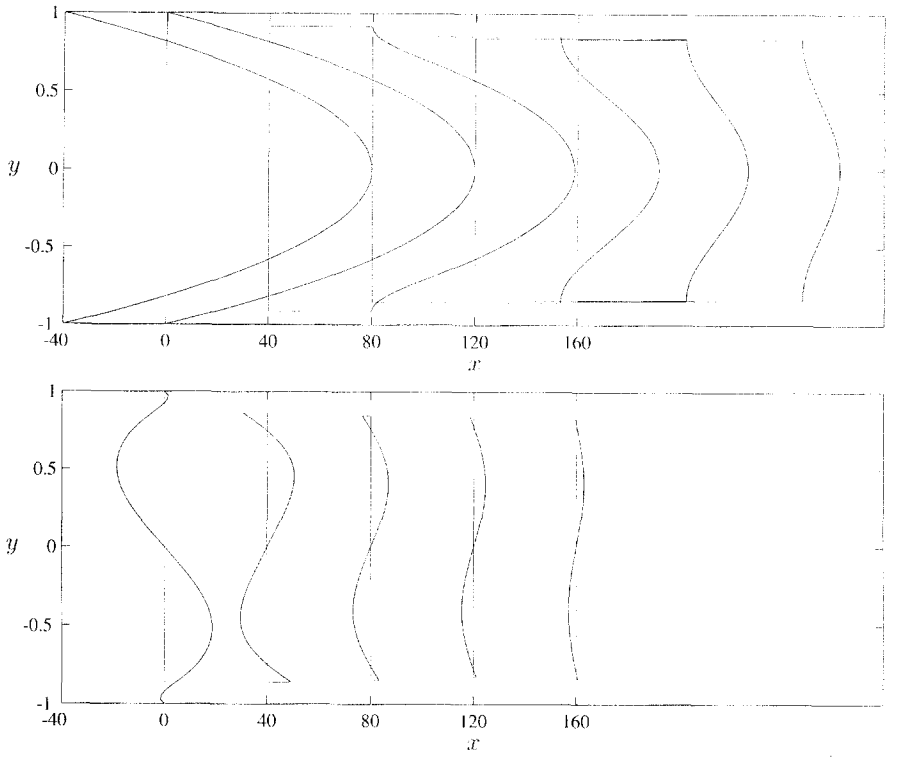

Fig. 5. – Velocity profile relaxation, $Re = 1000$, $1/We = 0$, $\hat{\rho} = 0$ and $\hat{\mu} = 0$. u-velocity (top) and v-velocity (bottom). v is here scaled up 500 times compared to u.

The outflow from a plane channel with an upstream fully developed Poiseuille flow can be seen in Figure 5. The figure shows the velocity distribution at several downstream positions for both the u and v components. The v velocity is several orders of magnitude smaller than the u velocity and is therefore multiplied by a factor of 500. The u profile at $x = -40$ represents the upstream boundary condition, the perfect parabola obtained in a plane Poiseuille flow. The normal velocity at this point is identically zero. These conditions are constant throughout the channel and the effect of the discharging jet appears within one channel height from the exit.

At the next position, $x = 0$ the profile represents the end of the channel, *i.e.* the nozzle edge. Here the streamwise velocity distribution has changed. The centreline velocity has decreased slightly and the profile is wider. This can also be seen by examination of the normal velocity distribution at the same point. This shows that fluid is transported from the centreline towards the walls. At the walls however, the normal velocity is directed towards the centre of the channel. When the fluid leaves the channel the boundary condition will change from no-slip to no-shear which will result in an acceleration of the fluid at the surface. The streamwise velocity at the surface is highest directly at the exit whereafter it decays.

At $x = 40$ the streamwise velocity at the surface is $0.8U_m$, and the jet has contracted which is a consequence of momentum and mass conservation. Also, the profile has inflection points and at all positions downstream the profiles are similar to this profile. Due to this relaxation process the deviation from a uniform velocity distribution decreases downstream.

3.3.1. *Similarity of the relaxation process*

In Figure 6 both velocity components, u and v, have been plotted against the η- and the y-coordinates. To the left in each graph the velocities are plotted as functions of the computational coordinate η and this clearly

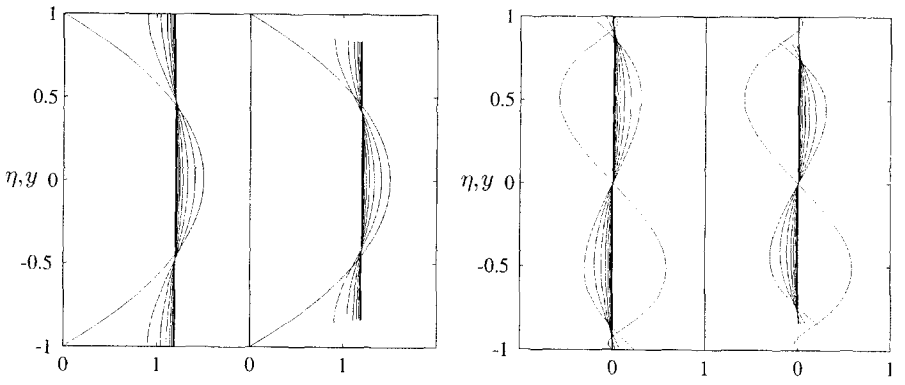

Fig. 6. – Velocity profile relaxation u (left) and v (right). Plotted against η and y, (left and right in each graph). The profiles start at $x = 0$ and continues with $\Delta x = 20$.

shows how the relaxation seems to occur with the two points at $\eta = \pm 0.48$ as fixed. These point seems to be more distinct for u than for v.

To the left in the graphs velocity profiles are plotted as functions of the 'real' coordinate y. Also in this figure there seems to be fixed points which are more distinct for u. This is, however, due to the contraction of the jet which is 'quicker' compared to the velocity relaxation. It should be noted that the v-velocity has been scaled up 500 times.

In Figure 7 the streamwise velocities at the surface and centreline of the jet are plotted against the scaled coordinate x/Re together with the location of the free surface for three Reynolds numbers, $Re = 100$, 1000 and 10000. For the two highest Reynolds numbers the graphs are identical, whereas the lowest Reynolds number shows a slight deviation.

3.3.2. *Varying entrance length*

In section 2.3 the entrance length needed to achieve a fully developed channel flow was discussed. From Figure 7 it is possible to find a relaxation length, ℓ_R, for the liquid channel jet. If this length is defined as the length from the end of the channel to the downstream location where $|u_{surface} - u_{CL}| < 0.01 u_{CL}$, then

$$\ell_R^u = 0.36\, xRe,$$

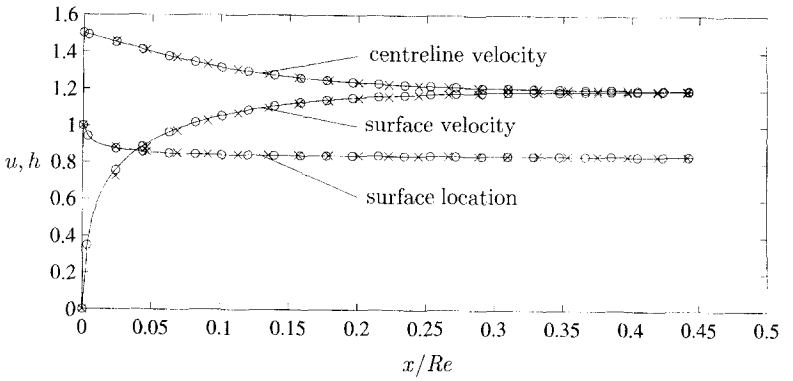

Fig. 7. – Velocity at the centreline and surface as well as the location of the free surface. (×) $Re = 100$, (○) $Re = 1000$; (—) $Re = 10000$, $\tilde{\rho} = 0$ and $\tilde{\mu} = 0$.

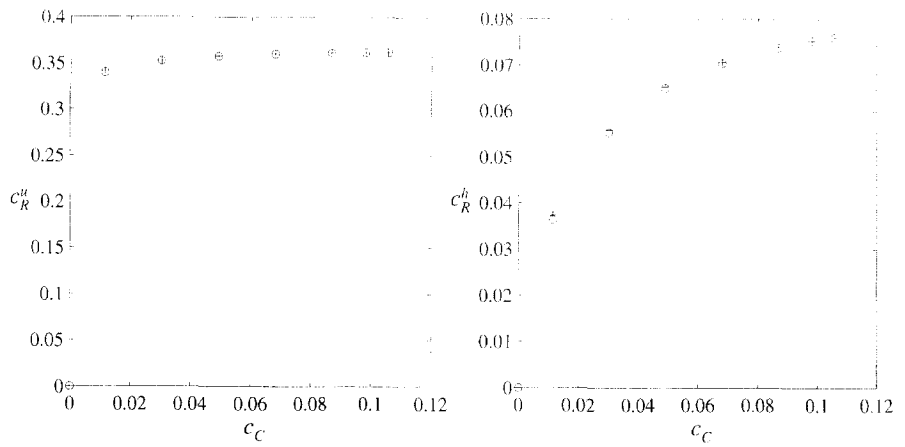

Fig. 8. – Relaxation length as a function of entrance length for the velocity profile (left) and surface location (right). (○) $Re = 1000$; (+) $Re = 10000$, $\tilde{\rho} = 0$ and $\tilde{\mu} = 0$.

where the superscript indicates velocity relaxation. This is necessary since the figure also shows a shorter distance to reach the final jet thickness compared to the distance required to reach velocity uniformity. The relaxation length for the free surface, ℓ_R^h, is defined as the downstream location where $|h - h_{final}| < 0.01 h_{final}$.

Calculations have also been performed for profiles at the end of the channel which deviate from the parabola. These profiles were obtained by starting the calculation with a uniform velocity distribution entering a channel. The velocity distribution at the end of the channel could be varied by changing the channel length at constant Reynolds number. The dimensional relations for the channel and relaxation lengths are given by

$$\ell_C = c_C \, aRe,$$
$$\ell_R^{u,h} = c_R^{u,h} \, aRe,$$

respectively, where a is the half channel height. The channel length, ℓ_C, was varied for two different Reynolds numbers, $Re = 1000, 10000$. Thus for given channel length there is one corresponding relaxation length $\ell_R^{u,h} = f(\ell_C)$, which can be seen in Figure 8. The graphs contain results for the velocity distribution and surface location. It should be pointed out that the points for $c_E = 0$ are not calculated but assumed to be valid since if there is no channel there will be no velocity profile relaxation and no change in surface location.

The velocity relaxation length is almost constant for channel lengths $\ell_C > 0.01 aRe$. This means that $Re = 1000$ gives $\ell_C \approx 10a$. Hence, with a channel only five channel heights long, the relaxation length is 170 channel heights. For a fully developed flow the relation between relaxation and entrance length is $\ell_R \approx 2.2 \ell_E$.

The free surface relaxation is more dependent of channel length than the velocity relaxation. Also, the relaxation length is markedly shorter. From the graphs it is clear that $\ell_R^u > 5\ell_R^h$. The maximum length relative ℓ_R^h is obtained if the flow is fully developed. Below $C_C \approx 0.07$ the surface relaxation length is longer compared to the channel length, and above it is shorter.

3.3.3. *Effect of a viscous ambient gas*

Up to this point the ambient gas has been assumed to be inviscid. Clearly viscosity will affect the flow of the jet, since it will result in a shear, *i.e.* drag, on the surface. In Figure 9 results are shown for a constant Reynolds number for the jet with $\tilde{\mu}$ varying. This figure shows a downstream jet expansion when the gas is viscous. The shear on its surface drains momentum from the jet and in order to preserve mass continuity the

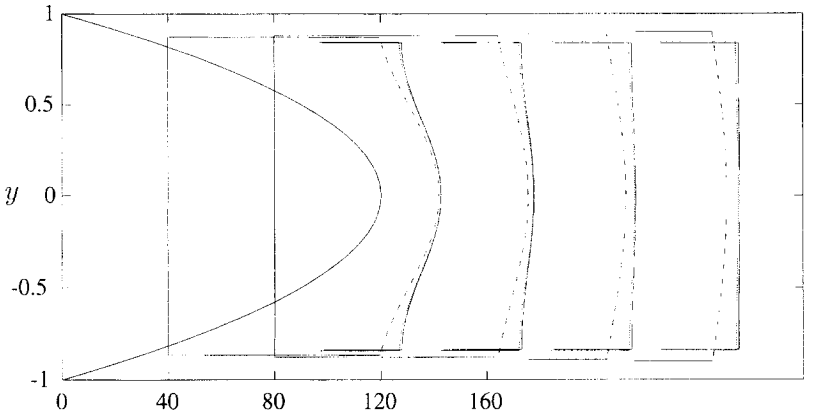

Fig. 9. – Velocity profile for $Re = 1000$. (solid) $\tilde{\mu} = 0.01$; (dotted) $\tilde{\mu} = 0.1$; (dash-dotted) $\tilde{\mu} = 10$. Positions for profiles, from left to right are $x = 0, 40, 80, 120, 160$.

mean velocity of the jet decreases. These effects becomes increasingly dominant when the viscosity ratio is increased. In the figure the density ratio is constant.

The asymptotic behaviour of the jet discussed in the previous section will clearly be influenced by the viscosity of the gas. For a viscosity ratio comparable to a water jet emanating into the air the effect of a viscous ambient gas is very small in the relaxation region, *i.e.* from the end of the channel to ℓ_R.

4. LINEAR STABILITY

The present flow visualisation results of plane liquid jets emanating from the plane channel flow nozzle, clearly show waves on the surface of the jet. These waves are initially homogenous in the spanwise direction. Hence, the disturbance is two-dimensional and independent of the spanwise coordinate.

The stability of the basic flow calculated in section (3), is investigated by temporal linear stability theory. Initially three-dimensional disturbances are considered, but calculations are restricted to two-dimensional travelling wave disturbances.

The basic flow is a function of both x and y, but the variation in the streamwise direction is assumed to be slow compared to the streamwise wavelength of the disturbance. This means that the basic flow can be assumed to be locally parallel, *i.e.* only dependent on the y-coordinate.

4.1. Linear stability equations

The velocity field can be divided into the basic flow field and the disturbance flow field such that

$$\mathbf{u} = \{U(y) + u'(x,y,z,t), v'(x,y,z,t), w'(x,y,z,t)\} \quad \text{and} \quad p = P + p'(x,y,z,t),$$

where the variables are scaled with the lengthscale taken to be local undisturbed jet thickness, local mean velocity and primes denote disturbance quantities. This decomposition can be inserted into the Navier-Stokes

equations (1) and (2), and after linearisation, *i.e.* neglecting terms that are quadratic in the disturbance quantities, this becomes

$$\frac{\partial u}{\partial t} + U\frac{\partial u}{\partial x} + vDU = -\frac{\partial p}{\partial x} + \frac{1}{Re^{l,g}_{local}}\nabla^2 u, \tag{21}$$

$$\frac{\partial v}{\partial t} + U\frac{\partial v}{\partial x} = -\frac{\partial p}{\partial y} + \frac{1}{Re^{l,g}_{local}}\nabla^2 v, \tag{22}$$

$$\frac{\partial w}{\partial t} + U\frac{\partial w}{\partial x} = -\frac{\partial p}{\partial z} + \frac{1}{Re^{l,g}_{local}}\nabla^2 w, \tag{23}$$

where the primes have been dropped [2] and $D = d/dy$. Similarly for the continuity equation

$$\frac{\partial u}{\partial x} + \frac{\partial v}{\partial y} + \frac{\partial w}{\partial z} = 0. \tag{24}$$

The Reynolds number $Re^{l,g}_{local}$ represents a local quantity but since the flow rate is constant in the jet this means that it will be constant in the channel and at all downstream positions in the jet. The scaling of the length and velocity variables in the jet will however change due to the contraction and increase of mean velocity in the downstream direction. This implies that when the whole jet is considered the results obtained at one streamwise position has to be converted to the 'global' scaling, *i.e.* the half channel height and mean velocity in the channel. The local Weber number will not be constant for all streamwise positions in the jet, since

$$We_{local} = \rho^l U^2_{m,local} a_{local}/\gamma = \rho^l Q U_{m,local}/\gamma.$$

Since the jet contracts the mean velocity will increase, hence the local Weber number will increase downstream.

The linearised momentum and continuity equations (21)–(24), can then be used to obtain an equation for the v-disturbance

$$\left(\frac{\partial}{\partial t} + U\frac{\partial}{\partial x}\right)\nabla^2 v - D^2 U\frac{\partial v}{\partial x} = \frac{1}{Re^{l,g}}\nabla^4 v. \tag{25}$$

Also, the free surfaces are perturbed from their basic state, $y = 1$,

$$\mathcal{H}_{+1}(x,y,t) = y - 1 - h_{+1}(x,t) = 0,$$
$$\mathcal{H}_{-1}(x,y,t) = y + 1 - h_{-1}(x,t) = 0,$$

which inserted into (2.1) give an equation for the disturbance of the free surface

$$\frac{\partial h_{\pm 1}}{\partial t} + U^{l,g}\frac{\partial h_{\pm 1}}{\partial x} = v^{l,g} \quad \text{at} \quad y = \pm 1. \tag{26}$$

4.2. Boundary conditions at the surface

The perturbed free surface is located at $y = 1 + h$ and the boundary conditions are linearised to $y = 1$. The streamwise velocity should be continuous across the surface,

$$u^l = u^g \quad \text{at} \quad y = 1 + h,$$

[2] Throughout the rest of this section uppercase letters indicate quantities related to the basic laminar flow field, and lowercase letters indicate disturbance quantities.

but if the basic flow is varying with y the condition becomes

$$u^l + hDU^l = u^g + hDU^g \quad \text{at} \quad y = 1, \tag{27}$$

where a series expansion of the basic flow around $y = 1$ has been performed, continuity has been used and terms quadratic in the disturbance quantities dropped.

In the normal and spanwise direction the basic flow is zero, hence v and w have to be continuous at $y = 1$,

$$v^l = v^g, \tag{28}$$

$$w^l = w^g, \tag{29}$$

where (28) gives the first boundary condition. Now, by taking $\partial/\partial x(27)+\partial/\partial z(29)$ and making use of continuity, a second condition for the v-disturbance can be formulated

$$\frac{\partial}{\partial y}(v^l - v^g) - \frac{dh}{dx}(DU^l - DU^g) = 0 \quad \text{at} \quad y = 1. \tag{30}$$

The stress conditions at the surface (11) are also linearised with use of the fact that the basic flow field satisfies the boundary conditions, and at $y = 1 + h$ these are written as

$$\frac{\partial v^l}{\partial x} + \frac{\partial u^l}{\partial y} + \frac{dU^l}{dy} = \tilde{\mu}\left(\frac{\partial v^g}{\partial x} + \frac{\partial u^g}{\partial y} + \frac{dU^g}{dy}\right), \tag{31}$$

$$p^l - \frac{2}{Re^l}\frac{\partial v^l}{\partial y} + \frac{1}{We}\left(\frac{\partial^2 h}{\partial x^2} + \frac{\partial^2 h}{\partial z^2}\right) = \tilde{\rho}p^g - \tilde{\mu}\frac{2}{Re^l}\frac{\partial v^g}{\partial y}, \tag{32}$$

$$\frac{\partial v^l}{\partial z} + \frac{\partial w^l}{\partial y} = \tilde{\mu}\left(\frac{\partial v^g}{\partial z} + \frac{\partial w^g}{\partial y}\right). \tag{33}$$

Conditions (31) and (33) can be reduced to one condition for the v-disturbance with the aid of continuity,

$$\left(\frac{\partial^2}{\partial y^2} - \frac{\partial^2}{\partial x^2} - \frac{\partial^2}{\partial z^2}\right)(v^l - \tilde{\mu}v^g) = \left(D^2U^l - \tilde{\mu}D^2U^g\right)\frac{dh}{dx}, \tag{34}$$

where the derivatives of the basic velocity fields in the liquid and gas are due to linearisation of the free surface location.

Finally, the pressure in (32) can be substituted by using the linearised momentum and continuity equations, (21), (22) and (23), which gives

$$\begin{aligned}\left(\frac{\partial}{\partial t} + U^l\frac{\partial}{\partial x}\right)\frac{\partial v^l}{\partial y} - \frac{1}{Re^l}\left(3\frac{\partial^2}{\partial x^2} + \frac{\partial^2}{\partial y^2}\right)\frac{\partial v^l}{\partial y} - \frac{\partial v^l}{\partial x}DU^l = \\ \tilde{\rho}\left(\frac{\partial}{\partial t} + U^g\frac{\partial}{\partial x}\right)\frac{\partial v^g}{\partial y} - \frac{\tilde{\mu}}{Re^l}\left(3\frac{\partial^2}{\partial x^2} + \frac{\partial^2}{\partial y^2}\right)\frac{\partial v^g}{\partial y} - \frac{\partial v^g}{\partial x}DU^g \\ - \frac{1}{We}\left(\frac{\partial^2}{\partial x^2} + \frac{\partial^2}{\partial z^2}\right)^2 h.\end{aligned} \tag{35}$$

4.3. Normal modes

The equations (25), (26) and the boundary conditions (28), (30), (34) and (35), are all linear in x and t, hence a normal mode ansatz can be made

$$v = \hat{v}(y)\exp\left[i(\alpha x + \beta z - \alpha c t)\right], \tag{36}$$

where $\hat{v}(y)$ is the amplitude function, c the phase speed and α, β the streamwise and spanwise wavenumbers respectively. By substituting (36) into the disturbance equations and accompanying boundary conditions the following system of equations is obtained,

$$(U-c)(D^2-k^2)\hat{v} - D^2U\hat{v} = -\frac{i}{\alpha Re^{l,g}}(D^1 - 2k^2D^2 + k^1)\hat{v} \tag{37}$$

$$\left.\begin{aligned}
i\alpha(U^{l,g}-c)\hat{h}_{\pm1} &= \hat{v}^{l,g} \\
\hat{v}^l &= \hat{v}^g \\
D\hat{v}^l - i\alpha\hat{h}_{\pm1}\left(DU^l - DU^g\right) &= D\hat{v}^g \\
(D^2-k^2)\hat{v}^l - i\alpha\hat{h}_{\pm1}\left(D^2U^l - \tilde{\mu}D^2U^g\right) &= \tilde{\mu}(D^2-k^2)\hat{v}^g \\
(U^l-c)D\hat{v}^l + \frac{i}{\alpha Re^l}(D^2-3k^2)D\hat{v}^l - DU^l\hat{v}^l &= \\
\tilde{\rho}(U^g-c)D\hat{v}^g + \tilde{\mu}\frac{i}{\alpha Re^l}(D^2-3k^2)D\hat{v}^g - \tilde{\rho}DU^g\hat{v}^g + \frac{ik^4}{\alpha We}\hat{h}_{\pm1} &
\end{aligned}\right\} \text{ at } y = \pm 1,$$

where $k^2 = \alpha^2 + \beta^2$ and $\hat{h}_{\pm1}$ are the amplitudes of the disturbance at the two surfaces. This gives an eigenvalue problem

$$\mathcal{F}(\alpha, \beta, c, Re, We) = 0, \tag{38}$$

which is solved for the complex eigenvalue $c = c_r + ic_i$, by choosing a fixed Reynolds number and real wavenumbers α and β. The real part c_r gives the phase speed of the disturbance and the imaginary part c_i together with the wavenumber gives the growth rate in time, αc_i. If $c_i > 0$ the flow is linearly unstable, *i.e.* the disturbance is growing in time.

As farfield boundary conditions in the gas the disturbance amplitudes, $\hat{u}$, $\hat{v}$ and $\hat{w}$, are set to zero. This gives

$$\hat{v}^g = 0 \quad \text{and} \quad D\hat{v} = 0 \quad \text{at} \quad y = \pm\infty.$$

Because of the symmetry of the basic flow with respect to the centreline of the jet, even and odd solutions to the eigenvalue problem can be treated separately [3]. This means that the eigenvalue problem can be solved in half the jet. The boundary conditions at the centreline are determined by the choice of even or odd solutions. The result of the eigenvalue problem is several different solutions, *i.e.* 'modes', which consist of eigenvalues with corresponding eigenfunctions $\hat{v}(y)$.

[3] A v-even solution is equivalent to anti-symmetric wave and *vice versa*, *see* Figure 1.

4.3.1. *Squire's theorem*

The equations describe a three dimensional disturbance, and (37) can with the aid of Squire's theorem be transformed to an equivalent two-dimensional problem. This can be seen from defining a new Reynolds number as $\widetilde{Re} = \alpha Re$, which for homogeneous boundary conditions would give an eigenvalue problem,

$$\mathcal{F}(k, c, \widetilde{Re}) = 0.$$

where k has replaced both α and β. By examining the linearised equation for the surface motion and boundary conditions it is clear that one can introduce new variables

$$\tilde{h} = \alpha \hat{h} \quad \text{and} \quad \widetilde{We} = \alpha^2 We.$$

With these additions Squire's transform applies to the free surface eigenvalue problem, (38),

$$\mathcal{F}(k, c, \widetilde{Re}, \widetilde{We}) = 0.$$

4.4. SOLUTION METHOD

There exist several solution methods for the eigenvalue problem generated by the linear stability theory, such as shooting methods that are used to find one single eigenvalue at the time, and methods that solve for the complete eigenvalue spectrum.

Here the eigenvalue problem has been solved with a spectral method, where the solution is represented as an infinite sum of Chebyshev polynomials,

$$\hat{v} = \sum_{n=0}^{\infty} b_n T_n(y), \quad \text{for} - 1 \leq y \leq 1, \tag{39}$$

where T_n is the n-th Chebyshev polynomial and b_n coefficients to be determined. The serie is truncated at some finite value N and inserted into the equation and boundary conditions which gives a linear system of the form

$$\mathcal{L}\mathbf{b} = c\mathcal{M}\mathbf{b},$$

where $\mathbf{b} = \{b_0, b_1, b_2, \ldots, b_{N-1}, b_N\}$ is the coefficient vector to the Chebyshev expansion (39). The matrices $\mathcal{L}$ and $\mathcal{M}$ are given by

$$\mathcal{L} = i\alpha U(\mathbf{T}'' - \alpha^2 \mathbf{T}) - i\alpha U'' \mathbf{T} - \frac{1}{Re^{l.g}}(\mathbf{T}^{iv} - 2\alpha^2 \mathbf{T}'' + \alpha^4 \mathbf{T}) \tag{40}$$

$$\mathcal{M} = i\alpha(\mathbf{T}'' - \alpha^2 \mathbf{T}), \tag{41}$$

where $\mathbf{T^{(k)}}$ is a matrix representing the k:th derivative of the Chebyshev polynomials. The zeros of the highest order polynomial are chosen as collocation points which gives

$$y_m = cos\frac{\pi m}{N}, \quad -1 \leq y \leq 1, \quad m = 0, 1, \ldots, N-1, N.$$

This will give a distribution with grid points clustered at the ends of the interval. The matrices (40) and (41) have dimension $(N+1) \times (N+1)$. To these are added the boundary conditions and the kinematic equation for the free surface. This is done for the liquid as well as for the surrounding gas and the conditions at the free surface will couple these matrices. The resulting general eigenvalue problem can be solved with standard

numerical methods. Here it was solved by the generalised eigenvalue solver, *eig*, built into the commercially available mathematical software *Matlab*.

4.5. Linear stability results for uniform jet flow

The stability of the plane liquid jet was analysed for various initial velocity profiles and parameter regions. However, first results from calculations for a jet with uniform velocity distribution are presented in order to compare with earlier reported results, (Li and Tankin, 1991). These results were obtained with the assumption of an inviscid ambient gas and a basic velocity distribution in the gas which is zero everywhere, *i.e.* there is a difference in the velocity for the gas and liquid at the surface.

In Figure 10 the growth rate is plotted as a function of wavenumber. For this case only one unstable even mode and one unstable odd mode exist. The figure contains one graph showing the growth rate for the even mode and one graph showing the growth rate for the odd mode at $Re = 63.2$. For this Re the even mode is the most unstable for all wavenumbers. This Reynolds number was chosen to be able to compare the numerical results directly with the results by (Li and Tankin, 1991). Hence, it is a way to validate the numerical solution method used here.

4.5.1. *The effect of a viscous ambient gas*

A viscous ambient gas will influence both the mean velocity distribution in the jet as well as the stability of the jet flow. If the viscosity ratio $\tilde{\mu}$, is small the influence on the mean velocity profile will be small, but the influence on the stability may still be large. This is due to the fact that in the inviscid case the source of instability is the pressure variation over the waves due to the velocity discontinuity at the surface. In the case of a viscous gas there will be a no-slip condition at the surface, which will change the boundary conditions for the disturbance and hence the stability.

In Figure 10 results are also plotted for a jet with a viscous ambient gas, $\tilde{\mu}$ =0.001, and a basic flow of the gas given by (14) in section 2.2. This small value of $\tilde{\mu}$ was chosen to exemplify the large effect of a viscous ambient gas. Since the basic flow of the jet is only slightly changed by the gas, it is assumed to be independent of the streamwise coordinate. To characterise the flow the thickness of the boundary layer in the surrounding gas is used. This is defined as δ_{99} and is taken at the position where the velocity of the gas is 1% of the mean velocity in the jet, U_m. Both the odd mode and the even mode are significantly damped for higher wavenumbers. From the figure it is also clear that for lower wavenumbers the viscosity in the gas may enhance the growth rate.

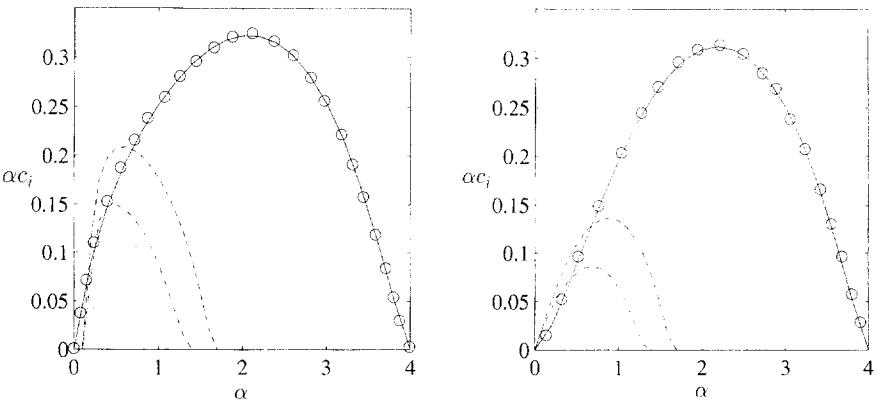

Fig. 10. – Growth rate as a function of wavenumber. $We = 40$, $Re = 63.2$, $\tilde{\rho} = 0.1$, (o) Data from [Li1991] and (–) calculation with inviscid ambient gas. Also, calculations with a viscous gas $\tilde{\mu} = 0.001$. (- -) $\delta_{99} = 0.023$, (- · -) 0.072 and (· · ·) 0.22. Even modes (left) and odd modes (right).

In the figure the growth rate is plotted for three different thicknesses of the boundary layer in the gas. This shows a growth rate which decreases when the thickness of the boundary layer is increased, which is equivalent to a reduced shear at the interface.

4.6. Linear stability results for viscous jet flow

The complete formulation of the stability problem for the plane liquid jet contains several parameters, Re, We, α, $\tilde{\mu}$ and $\tilde{\rho}$. It also depends on the downstream position as well as the inlet length for the basic flow. The effect of all parameters can not be investigated and the results presented are based on the flow of a water jet in air. This means that $\tilde{\mu}$ and $\tilde{\rho}$ will be kept constant. For $T = 20°C$ the viscosity for water is $\mu^l = 1.01 \cdot 10^{-3}$ kg/ms and for air $\mu^g = 1.79 \cdot 10^{-5}$ kg/ms, which gives a viscosity ratio $\tilde{\mu} = 0.0177$. Similarly for the density $\rho^l = 997$ kg/m^3 and $\rho^g = 1.21$ kg/m^3, which gives $\tilde{\rho} = 1.21 \cdot 10^{-3}$. The surface tension was set to be $\gamma = 0.070$ N/m. Changes in Reynolds number is achieved by a change in velocity. The increase in Reynolds number will then give an increasing Weber number.

4.6.1. *Stability of the fully developed channel flow jet*

Figure 11 shows unstable regions for a plane liquid jet emanating from a channel with an upstream parabolic velocity profile. In the figure results for five different Reynolds numbers are shown, $Re = 125$, 250, 500, 1000 and 2000. The vertical axis in the graphs represents the 'global' wavenumber and the horizontal axis the streamwise position scaled with the Reynolds number. As the velocity distribution scales with x/Re, it is also convenient to present the stability diagrams as function of this variable.

The jet is unstable in the shaded region of the figures with a growth rate indicated by contour curves. The figure shows even modes (left column), as well as odd modes (right column). When the Reynolds number is increased the shaded regions grows. It should be noted that an increase in Reynolds number gives that for a constant x/Re the x-position moves downstream.

Three different unstable anti-symmetric (even) modes can be found in Figure 11. The unstable regions for these modes partially overlap and are difficult to separate. However, one of these three even modes appears as a bounded region with a centre at $\alpha \approx 1.5$. This mode becomes unstable a distance downstream the nozzle and becomes stable again further downstream. In Figure 12 the locations of the different modes are given qualitatively. The bounded mode corresponds to region *III*.

This bounded region is most obvious for the lowest Reynolds number, $Re = 125$. As the Reynolds number is increased both the upstream end and maximum of the region moves towards higher x/Re. It also expands in the wavenumber direction and its maximum growth rate increases to $Re = 1000$, after which it decreases.

There is no similar region for the odd modes. However, if this bounded region of instability for the even modes is excluded, the graphs for the two remaining even modes are similar to the graphs for the odd modes. The qualitative location for these modes are given by regions *I* and *II* in Figure 12.

For $Re = 125$ the regions given by *I* and *II* are concentrated to the lower left corner, *i.e.* close to the nozzle and to low wavenumbers. When the Reynolds number is increased region *I* grows towards higher wavenumbers and further downstream. The slope from high growth rate to no growth at all is very steep which can be seen since the contour curves are stacked together in this region. For $Re = 2000$ and $\alpha > 0.5$ the region seems to be parallel to the vertical axis. This is not the case since for higher wavenumbers than those shown in the graph, the growth rate decreases. Maximum growth in this region is found at $\alpha \approx 1.5$. The second branch, *i.e.* the region orientated along the x/Re-axis, also expands for higher Reynolds numbers and becomes parallel to the axis for $x/Re = 0.2$. However, it seems to extend somewhere from the middle of the α-axis in the

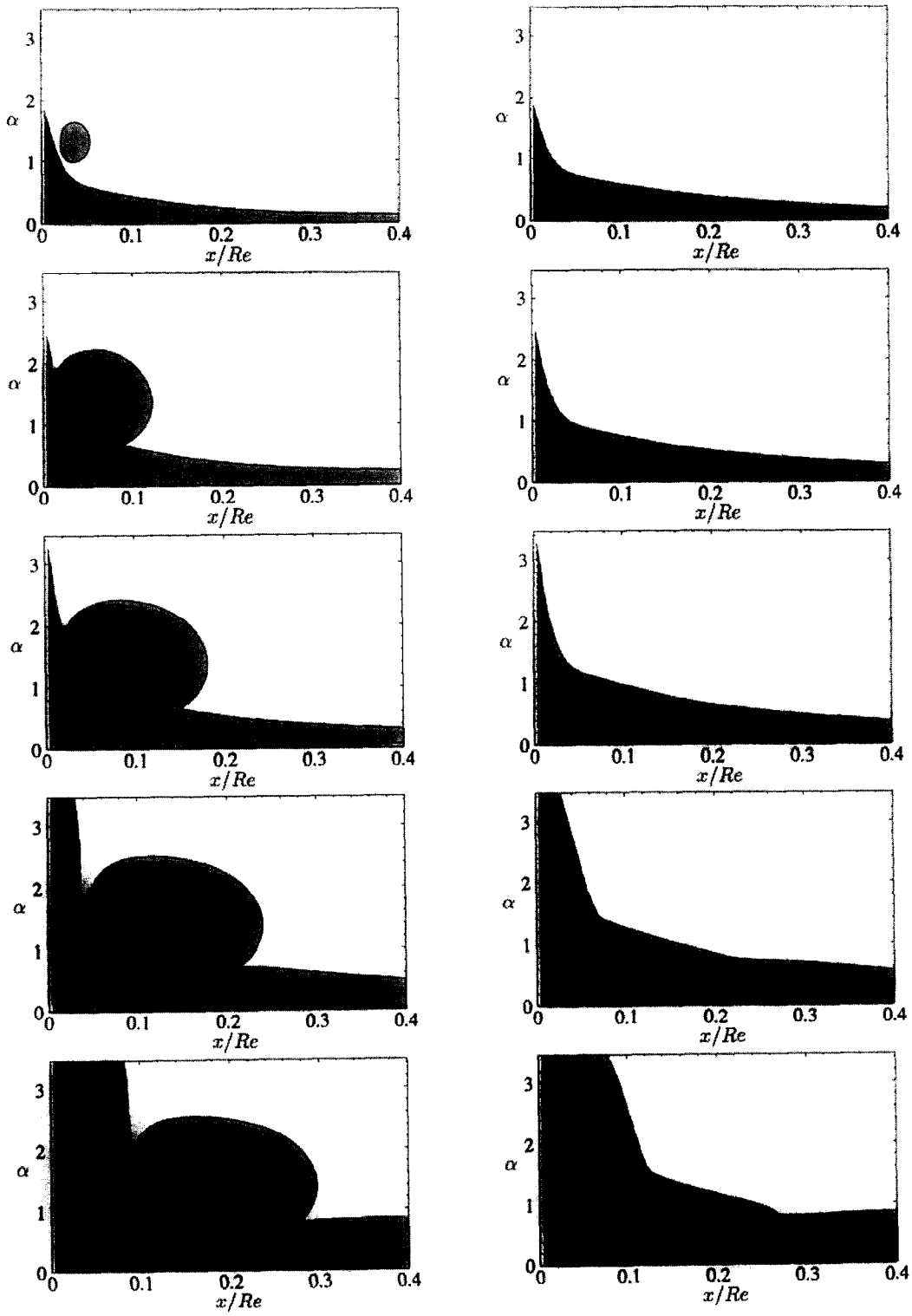

Fig. 11. – Unstable regions for a plane liquid jet surrounded by a viscous gas emanating from a channel. The shaded area indicates an unstable region. Also, the growth rate is indicated by contours of constant growth rate, $\Delta\alpha c_i = 0.005$. The left column contains results for the even modes and the right column result for the odd modes. From top to bottom Re = 125, 250, 500, 1000, 2000 and We = 0.432, 1.73, 6.91, 27.7 and 111.

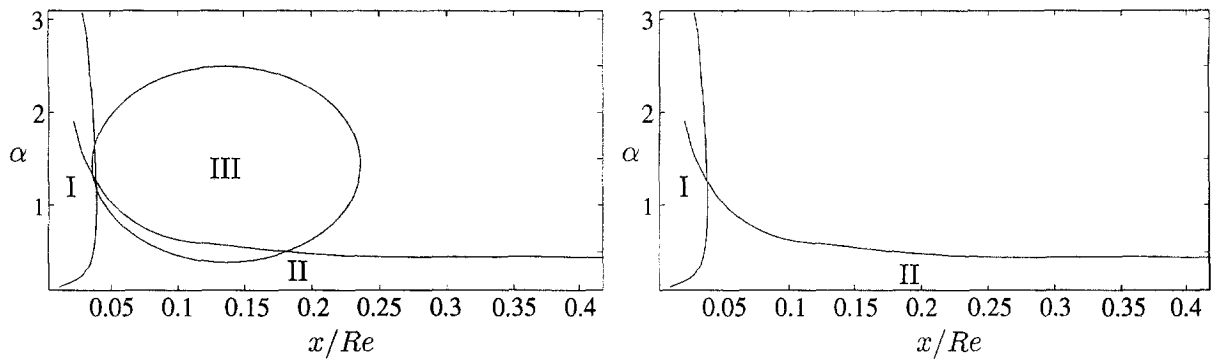

Fig. 12. – Qualitative description of the location of the unstable modes in figure 11. Even modes (left) and odd modes (right).

graph. The unstable region for the odd modes has a similar behaviour but the area of the region is larger and the maximum growth rate is lower.

To investigate the effect of the velocity profile on stability, the profiles at four positions, $x/Re = 0.037$, 0.069, 0.149, 0.306 were examined with respect to wavenumber and Reynolds number. The velocity profiles can be seen in Figure 13 and the corresponding stability diagrams in Figure 14 where the vertical axis of the graphs represents the 'local' wavenumber, *i.e.* scaling is performed with the local jet thickness, and the horizontal axis represents the Reynolds number, Re. As for Figure 11 even and odd modes are shown, and the unstable regions are shaded. The qualitative location of the modes can be found in Figure 15.

The first position chosen was at $x/Re = 0.037$. This represents a position where the free surface location is still changing. Consider first the even modes. For the lowest Reynolds number shown, $Re = 100$, there is an unstable region *II* for $\alpha < 0.6$. When the Reynolds number is increased the growth rate increases and region *II* extends towards higher wavenumbers. For a Reynolds number only slightly higher a second unstable region *III* can be seen. This is the same region as the bounded region found in Figure 11, and the maximum is found at $\alpha \approx 1.5$ and $Re \approx 400$. Behind this the low wavenumber region *II* can be seen extending to higher wavenumbers with increasing Reynolds number. For $Re \approx 1000$ the third unstable region *I* can be identified. The growth rate

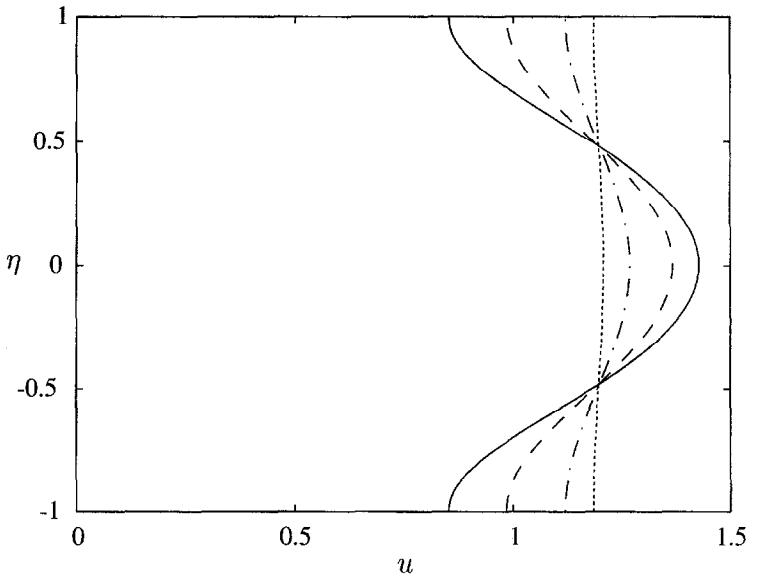

Fig. 13. – Streamwise velocity profiles for the four positions in figure 14. (—) $x/Re = 0.037$, (- -) 0.069, (- · -) 0.149, (· · ·) 0.306.

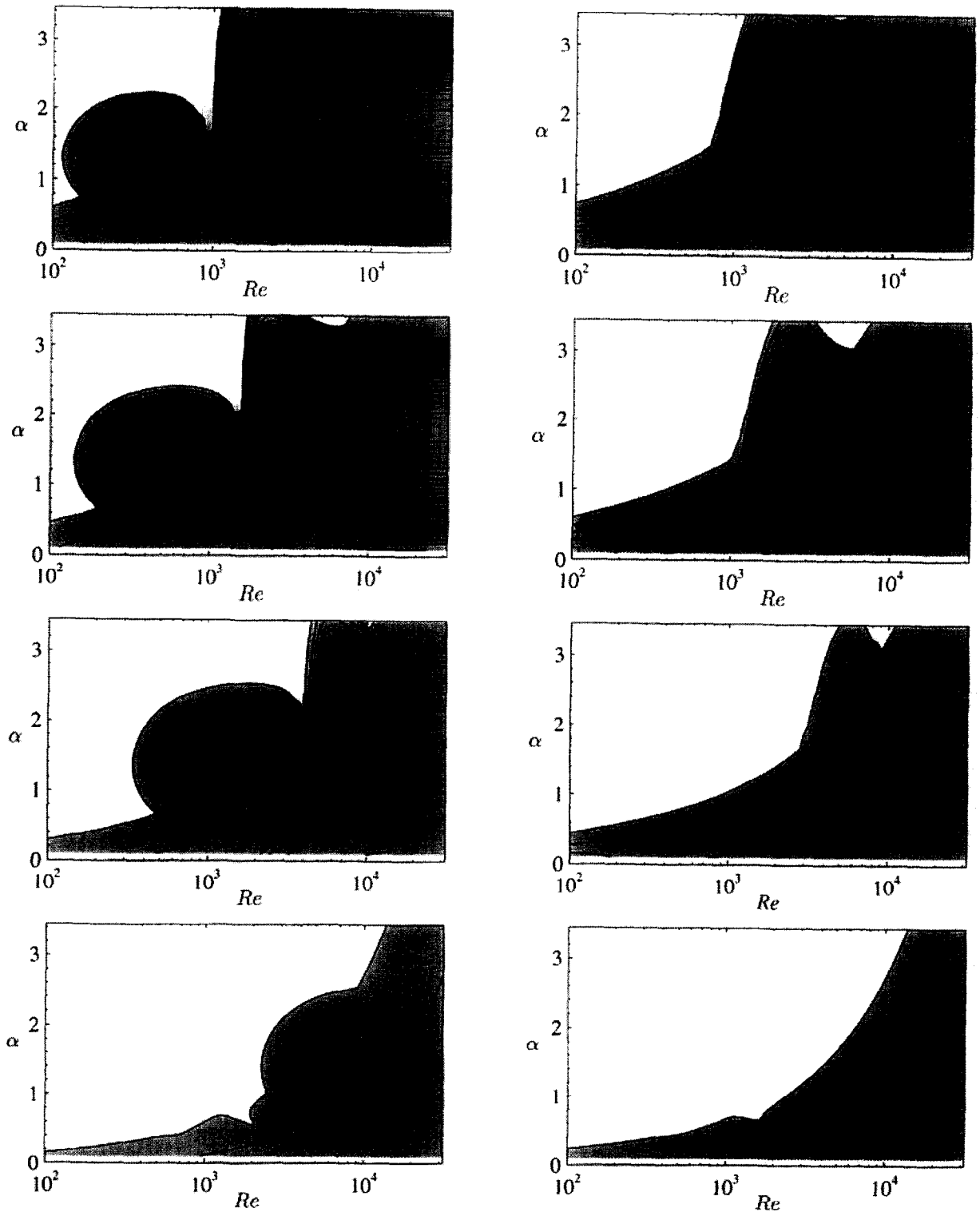

Fig. 14. – The maximum growth rate as a function of Reynolds number for four positions in the jet with a fully developed Poiseuille flow inside the channel. Distance between two contourlines $\Delta\alpha c_i = 0.005$. The left column contains the v-even modes and the right odd modes. From top to bottom $x/Re = 0.037,0.069,0.149,0.306$. The Weber number depends quadratically on the Reynolds number, $We = 2.77 \times 10^{-5} Re^2$.

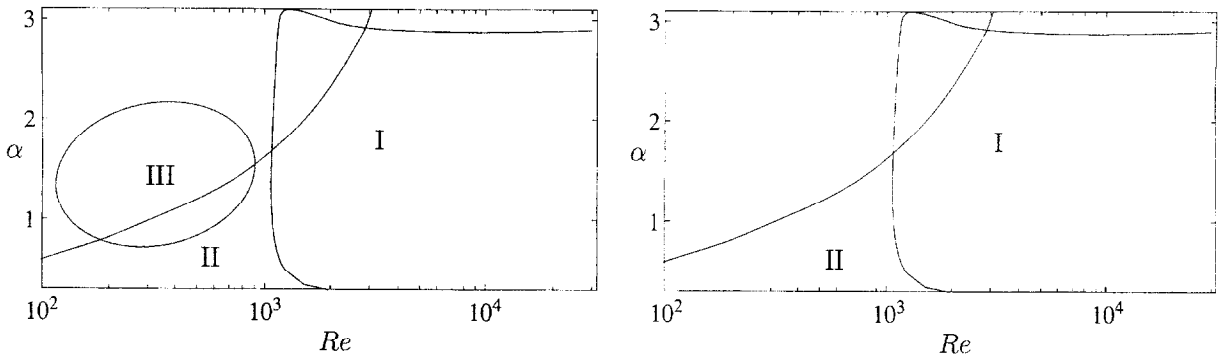

Fig. 15. – Qualitative description of the location of the unstable modes in figures 14. Even modes (left) and odd modes (right).

for this region increases quickly with Reynolds number, and the maximum growth is found at $\alpha \approx 1.9$. For the odd modes a similar behaviour can be found for both regions *I* and *II*. Also, mode *I* was followed for higher Reynolds numbers where the growth rate seems to be unaffected by the change in Reynolds number.

For the velocity profile at $x/Re = 0.069$ the growth rate for all regions has decreased. All regions have also moved towards higher Reynolds numbers. To the next position at $x/Re = 0.149$ the decrease is continued. Especially the growth rate in region *I* has decreased for both the even and the odd mode.

The lowest graphs represent $x/Re = 0.306$,where region *I* has totally vanished while region *III* still can be seen now starting at $Re \approx 2500$. For all four position the extent of region *II* only changes slightly.

In Figure 16 the flow of the ambient gas is the same as for Figure 14. However, the velocity distribution in the jet is uniform and assumed to be unaffected by the gas. As can be seen in the figure only one type of mode is unstable, *i.e.* one pair (even+odd). By comparison between Figures 14 and 16 it is clear that this mode is almost independent of the velocity distribution.

4.6.2. *Amplitude distribution of the disturbance*

The separation of the modes in the unstable regions has been made by examining the eigenvalue spectra and the eigenfunctions. An example can be seen in Figure 17. The figure contains six graphs with the upper left graph representing the eigenvalue spectrum. The horizontal axis represents the real part of the eigenvalues, which is the same as the phase speed, c_r, and the vertical axis represents the growth rate, αc_i. It should be remembered that the velocity is normalised with the mean velocity of the jet. An eigenvalue above $\alpha c_i = 0$, corresponds to a growing disturbance.

Five more graphs are shown in the figure, and these represents the eigenfunctions for five different eigenvalues. Those graphs are marked, $e_{I,II,III}$ and $o_{I,II}$, corresponding to the eigenvalue with the same marking in the eigenvalue spectrum. The eigenvalues are related to Figures 11, 14 and 16 through the subscripts *I*, *II* and *III*, whereas e indicates an even mode and o an odd mode. The vertical axis in these graphs represents the y-axis, with the location of the centreline at $y = 0$ and the free surface at $y = 1$. In the graphs the u-disturbance amplitude is given as a solid line and the amplitude for the v-disturbance as a dash-dotted line. At the top of each of those five graphs the corresponding eigenvalue is presented with phase speed c_r and growth rate αc_i.

Figure 17 is representative for region *II*, and maximum growth rate is found for mode o_{II}. The eigenfunction corresponding to this mode gives a maximum disturbance velocity at the surface, both for the normal as well as for the streamwise velocity. For the corresponding even mode maximum is found at the centreline. The mode corresponding to region *III* has a u-maximum at the inflection point and the v-maximum at the centreline. Also, the v-disturbance velocity is close to zero at the surface for e_{III}.

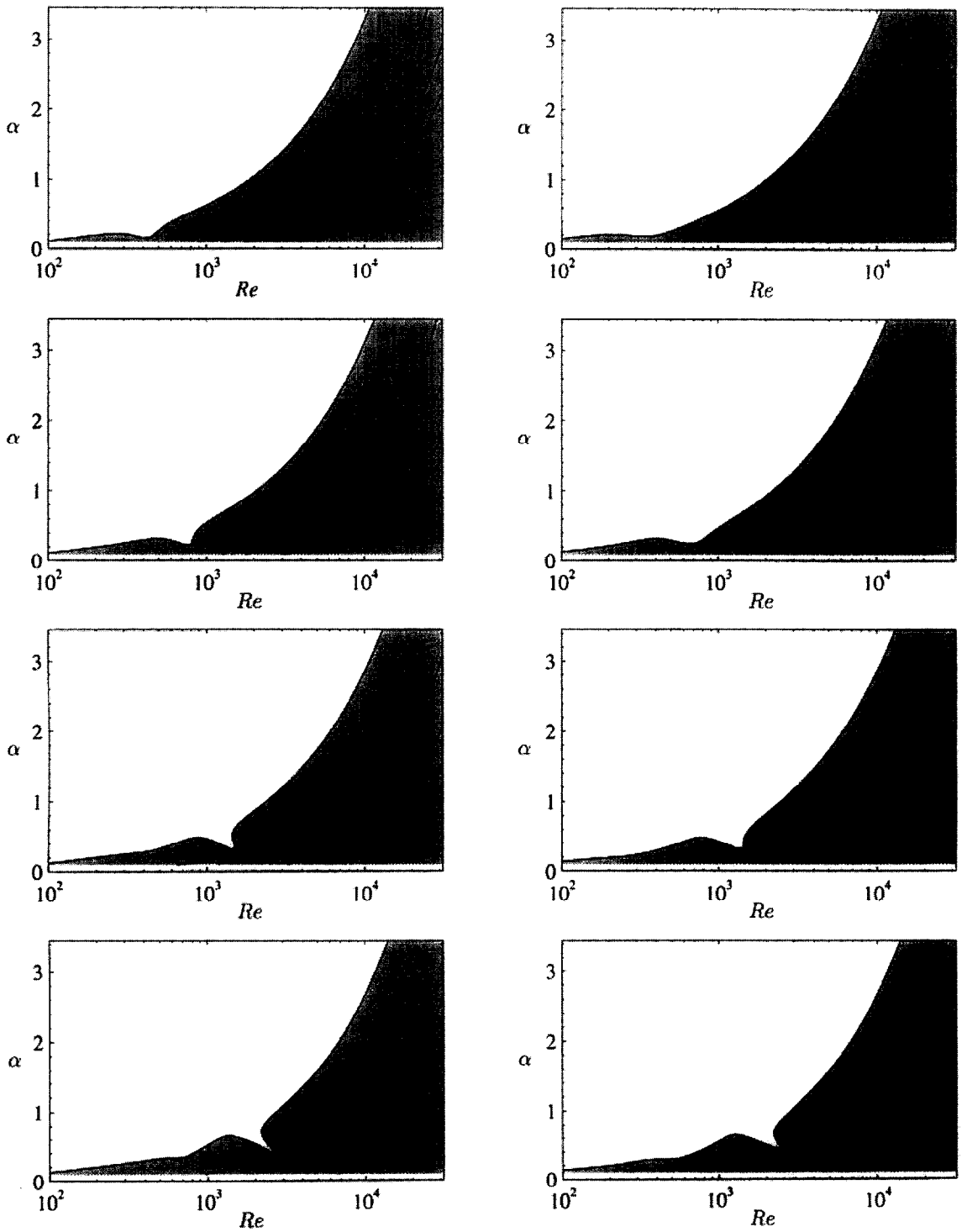

Fig. 16. – The maximum growth rate as a function of Reynolds number for four positions in a uniform jet with viscous ambient gas. Distance between two contourlines $\Delta\alpha c_i$ =0.005. The left column contains the v-even modes and the right odd modes. From top to bottom x/Re = 0.037, 0.069, 0.149, 0.306. The Weber number depends quadratically on the Reynolds number, $We = 2.77 \times 10^{-5} Re^2$.

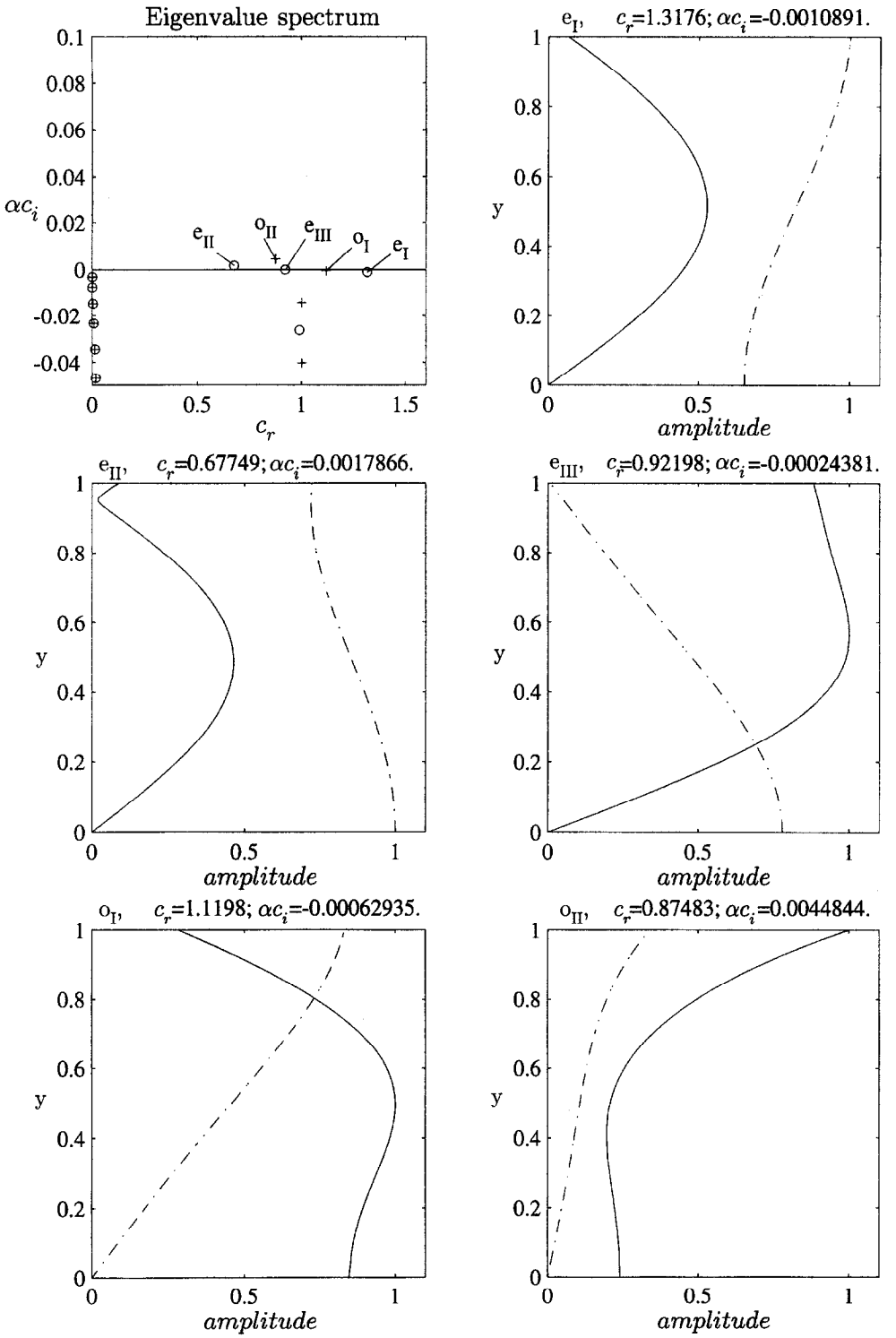

Fig. 17. – Eigenvalue spectrum and eigenfunctions for $x/Re = 0.149$. $Re = 1000$, $We = 25.1$ and $\alpha = 0.3$ (region *II*). (o) v-even and (+) v-odd modes. (—) u-amplitude and (- · -) v-amplitude. Calculated with a non-uniform velocity profile and viscous ambient gas. Normalisation of eigenfunctions is made with $max(\hat{u}(y), \hat{v}(y))$.

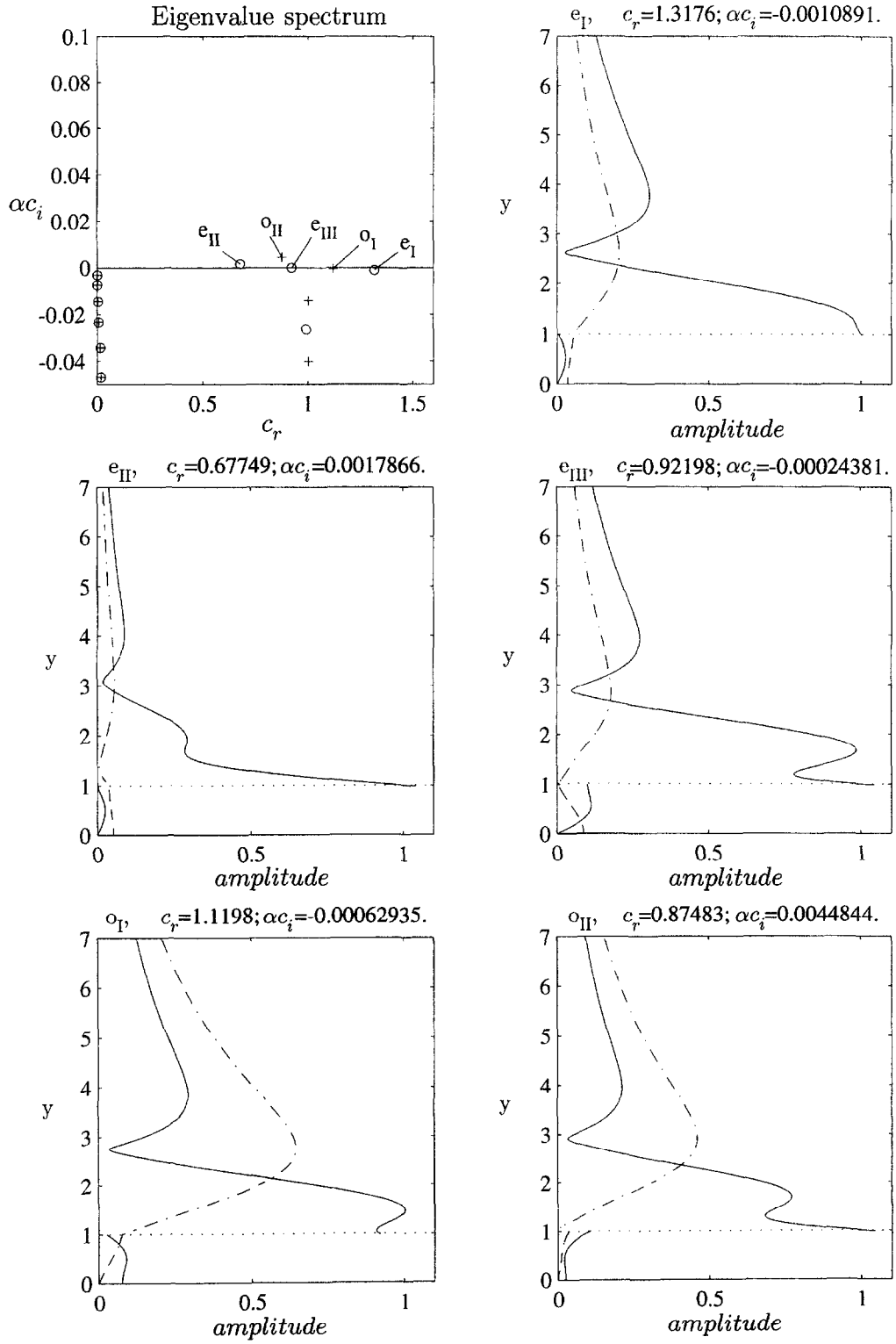

Fig. 18. – Eigenvalue spectra and eigenfunctions for the same parameters as figure 17, but with the eigenfunctions in the gas visible.

The calculation includes the ambient gas and Figure 18 shows the disturbance amplitude distributions with the same parameters as Figure 17. However the vertical scale has changed which allows for the amplitude of the disturbance velocities distributions in the air to be seen. As a result of the boundary conditions the v-disturbance velocity is continuous across the surface. Also, the amplitude of the streamwise velocity disturbance at the surface is larger in the gas than in the liquid. All modes are damped for $y \to \infty$.

5. Experimental set-up

5.1. Flow loop and nozzle

Two different types of plane water-jets have been produced with the apparatus shown in Figure 19. The apparatus consists of three main parts, the headbox where the nozzle is mounted, the dump tank and the submerged centrifugal pump. The flow rate was adjusted with a valve downstream the pump. The maximum flow rate of the pump is 340 l/min and the maximum pressure head 125 kPa. The jet width at the outlet is 150 mm and with a 2 mm jet it is possible to obtain a jet velocity of 11 m/s but for a larger jet thickness the velocity is reduced. The maximum obtainable Reynolds number based on jet thickness is around $25 \cdot 10^3$.

The water is fed from the pump to the headbox through a hardened PVC hose which is connected to a stiff PVC tube just upstream the headbox. The PVC-tube was divided into two before entering the headbox. To minimise vibrations the headbox was tightly fixed to a heavy workshop machinery tripod standing directly on the basement floor. In order to damp pressure pulsations in the system a small air pocket was kept at the top of the supply loop.

The headbox had the dimensions 25x25x15 cm^3 and was made of Plexiglas allowing optical access to its interior. At the outlet of the headbox different nozzle geometries can be inserted. The two nozzles used in this study were a two-dimensional *vena contracta* type and a plane channel nozzle which will produce a more or less fully developed plane Poiseuille flow. The spanwise width of the nozzles was 15 cm. Due to surface tension acting on the free rims of a plane jet, the jet tend to contract in the spanwise direction, *see* e.g. (Taylor, 1959). To avoid this and in order to ensure the two dimensionality of the jet, the sides of the jet were prevented to contract by letting side walls extend 20 cm beyond the nozzle exit. The orientation of the jet was chosen such that the jet emanates vertically to simplify shadowgraph visualisations and to avoid a bending of the jet by gravity.

The jet flow quality depends on the upstream conditions in the headbox, such as flow inhomogeneities and turbulence level and scales. In order to reduce such disturbances the water, when entering the headbox, had to pass a flow distributor consisting of a 30 mm thick bed of packed 4 mm diameter glass beads. Downstream this distributor the flow passed two fine meshed screens which reduce the turbulence level and also give a pressure drop which helps making the flow uniform. Downstream the screens a 6 cm long honeycomb with a cell diameter of 5 mm aligns the flow. Finally a screen was mounted as an arc with the top directed in the flow direction. This made it possible for air bubbles to move up to the sides at start up of the flow loop. Air bubbles did however easily get stuck at this screen and therefore it was possible to manually vibrate the screen by inserting a bar from the nozzle opening. The last screen had a porosity of 0.60 and for all velocities the Reynolds number based on wire diameter was less than 10 and hence this final screen was subcritical. The arc-shape of the screen will redirect the flow slightly and this will have some effect on the velocity distribution in the jets but the effect is assumed to be negligible. A pressure transducer was mounted on the wall of the headbox downstream the last screen and the transducer output was calibrated against the jet flow rate.

The slit nozzle consisted of two 5 mm thick brass pieces which were machined sharp at the outlet side. Their position could easily be adjusted in order to change the slit width.

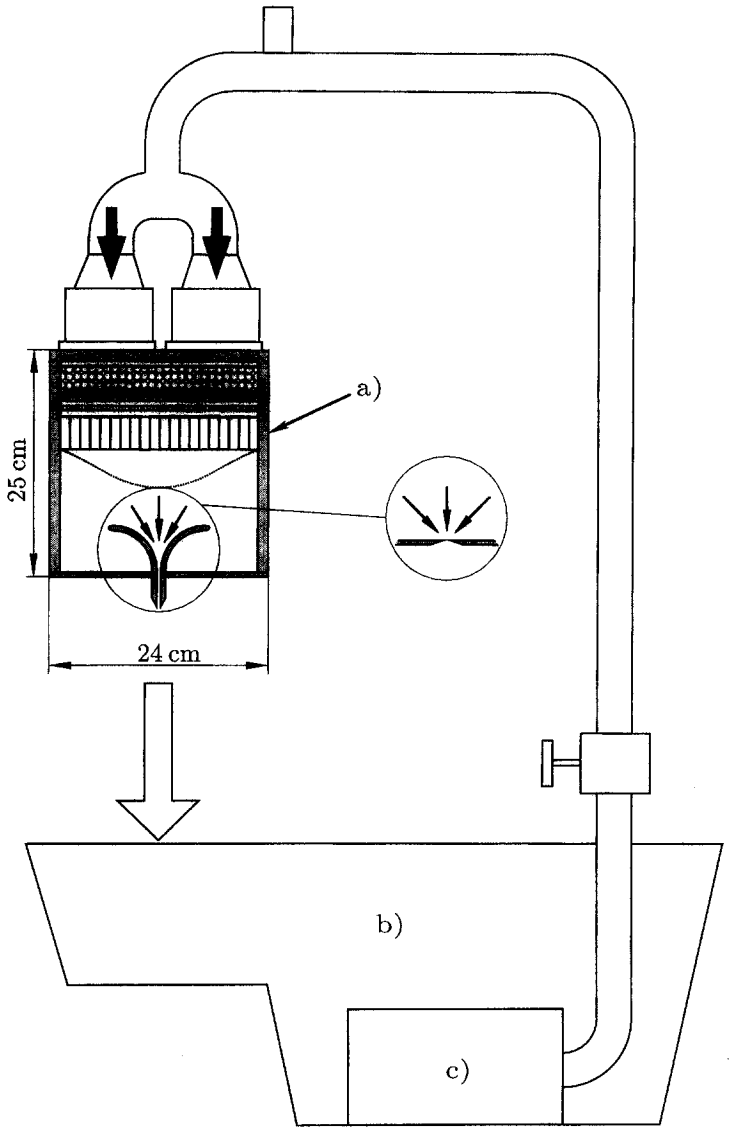

Fig. 19. – Experimental setup, a) head box, b) dump tank, c) centrifugal pump.

The channel nozzle consisted of a contraction made of two quarter cylinders with a radius of 5 cm followed by two 4 cm long flat plates, all made of brass. Also for this nozzle the channel width could be varied.

Both nozzles were carefully polished before performing any experiments. The sharp edges were checked regularly to ensure that they had no damages which could disturb the jet. Damage to the edges (or even a water droplet stuck at the outlet) showed up in the visualisations as a stationary wave pattern on the surface having a Λ-shape with the origin at the edge.

The flow of the gas surrounding the jet will influence the flow of the jet. With the present design of the nozzles and headbox the air flow should be similar for the two different orifices tested.

5.2. Flow visualisation

Two different methods have been used to visualise the flow of the plane jet, namely the shadowgraph method and reflective flakes (iriodin) seeded in the water. For both methods the images have been processed to obtain not only qualitative but also quantitative information.

5.2.1. *Shadowgraph method*

For the shadowgraph method, Figure 20 *i*, the jet was illuminated from one side by an ordinary slide projector standing 5 m from the jet. The distance should be as large as possible since the light source ideally should approximate a point light source. When the light from the projector pass through the jet any curvature of the surface of the jet, will give rise to a deflection of the light. This will be seen as a pattern of shadows on a semi-transparent plate which is mounted on the other side of the jet. This pattern corresponds to the irregularities on the surface of the liquid jet. The sharpness of the pattern depends on the distance between the jet and plate, and a shorter distance gives a sharper picture. The semi-transparent plate had vertical and horizontal centimeter markings in order to simplify measurements in the shadowgraph image.

5.2.2. *Reflective flakes*

Reflective flakes were used to visualise phenomena inside the jet. These flakes react to the shear, and tend to orient along stream surfaces. In order to detect a gradient in the flow, only a small concentration of the flakes is needed. The jet was then illuminated with a laser sheet, Figure 20.

The laser sheet was created by letting the laser beam from a 10 mW semi-conductor laser pass through a glass cylinder. The light sheet was led into the jet from the side, Figure 20 *ii*, and the light sheet had a thickness of approximately 1 mm, which allowed an illumination of the core of the jet. A black non-reflecting curtain was used as a background to improve the contrast.

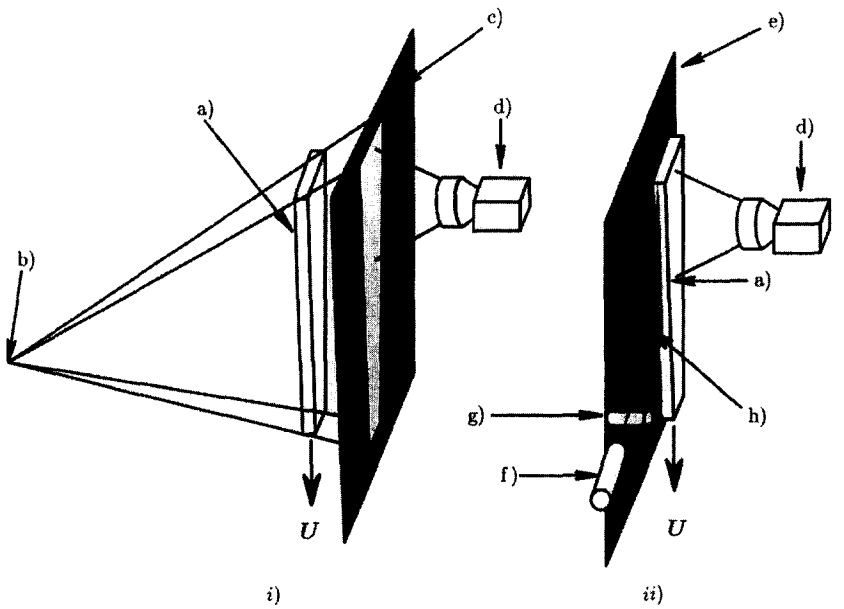

Fig. 20. – Visualisation set-ups. i) shadowgraph; ii) particle visualisation with a light sheet from the side. a) liquid jet, b) light source, c) semi-transparent plate, d) camera, e) black background, f) laser, g) glass cylinder and h) laser sheet.

5.2.3. *Video recording and photography*

Both the shadowgraph and particle visualisations were recorded. Photos of the visualisations were taken by an Olympus OM-2 camera with 35 mm black and white as well as colour slide film. Also, video recordings were made with a greyscale CCD-camera and a Hi8 video recorder. The use of video allows transient events to be captured as long as the speed of these is not too high. To improve the time resolution further a high-speed CCD-camera (Kappa 100) was used. This allowed sequences to be captured at up to 500 frames per second.

5.2.4. *Image processing*

To determine the wave length of the wave disturbance accurately, image processing of the video recordings was made. Frames from the video recording of the shadowgraph visualisation were transferred to a *Macintosh PowerPC/8500* computer via a *Scion LG-3* frame grabber card. From each frame a small strip (typically 10 pixels wide) representing the centre of the jet was extracted and transferred to the numerical software *Matlab*. To remove noise, the images were averaged in the spanwise direction. The result was a signal with a clear waveform. This signal was then divided into overlapping sequences and the streamwise length of these was typically a few wavelengths. However the background light intensity varied almost linearly in the streamwise direction and therefore the following expression for the intensity variation, $I(x)$, was fitted to the data in the least square sense,

$$I(x) = A\sin(kx + \varphi) + Bx + I_m.$$

Here A is the amplitude of the wave, k the wavenumber, φ the phase, B the coefficient for the linear trend of the intensity and I_m the mean intensity in the image. Since this was made on a series of sequences for different streamwise positions, the downstream development with x of the wavenumber could be found. In order to improve the accuracy this was done for 50-100 consecutive frames, and the results were averaged. From the wavenumber the wave length and the phase speed of the waves (knowing their angular frequency) could easily be obtained.

5.3. VELOCITY MEASUREMENTS

Velocity measurements in the jet were made both to determine the mean flow development and to investigate the disturbance flow. The mean flow measurements were made with a Pitot tube, whereas the time dependent velocity measurements were made with hot wire anemometry.

5.3.1. *Pitot tube measurements*

Jet velocity profiles were measured with a Pitot tube constructed from a small stainless steel tube. The original tube had inner and outer diameters of 0.4 mm and 0.6 mm, respectively. To reduce the spatial dimension of the Pitot tube tip the tube was flattened and sharpened at its end, resulting in an inner opening of 0.08 mm and an outer width of 0.2 mm. Special care was taken to ensure that the edges of the hole were sharp and this was checked with a microscope. The probe could be manually traversed through the jet. The pressure measured with the Pitot tube was transmitted by PVC-tubes to a differential pressure transducer. The pressure transducer measured the difference between the total pressure from the Pitot tube and the atmospheric pressure, which was assumed to be the same as the static pressure in the jet.

It was necessary to ensure that there was no air present in the tubing from the Pitot tube to the pressure transducer, which otherwise could have an effect on the pressure reading. The lack of air in the pressure sensing system was possible to determine not only by the transparency of the tubes, but also by monitoring the adjustment time when subjected to a change in pressure. When fully functioning the response time was less

than 0.5 s, but if an air bubble entered the system this time increased dramatically. The Pitot tube and pressure transducer were calibrated against a known height of water before and after the measurements.

5.3.2. *Hot wire anemometry measurements*

Hot wire anemometry was used to determine the amplitude and phase distributions of the travelling wave disturbance. The anemometer used was a *Dantec M01* and the hot film probe was the boundary layer type R15. It has a cylindrical sensor with a diameter of 70 μm and a sensing length of 1.25 mm. The hot film probe could be traversed through the jet with the same traversing mechanism as used for the Pitot tube measurements.

To obtain absolute measurements from hot wire anemometry the anemometer system has to be calibrated. However, since the procedure to obtain absolute readings is quite cumbersome since hot film anemometry in water is subjected to various sources of drift, it was decided to only obtain relative readings of the wave amplitude. If the amplitude of the fluctuating signal is small the relation between the signal from the anemometer and the velocity can be assumed to be linear. This can easily be seen from the King's law expression given by

$$U = k_1(E - E_0)^{1/n},$$

where E is the output from the anemometer at U velocity, E_0 the output at zero velocity, and k_1 and n constants determined by calibration. A series expansion around the voltage E at the velocity U gives that a small change in velocity Δu is related to a small change in voltage $\Delta e \ll E - E_0$ as

$$\Delta u \sim \Delta e.$$

The experimental set-up to determine the wave characteristics can be seen in Figure 21. The hot film probe was traversed through the jet at a distance of 20 mm downstream of the nozzle. The waves were triggered by a loudspeaker mounted on the nozzle and a signal generator was used to drive the loudspeaker at a fixed frequency. The signal to the speaker was sampled to a Macintosh Classic computer simultaneously as the signal from the anemometer by a *GW Instruments, inc. MacAdios-adio* A/D-converter. By traversing the probe through the jet and sample at a number of locations the phase of the disturbance could be found by using the generator signal as reference.

6. Experimental results

Measurements of the streamwise velocity distribution and flow visualisations were made with both the channel and the slit nozzle. The results showed significant differences in the behaviour of jets emanating from these nozzles. Special emphasis was put on the development of the wave instability which was studied both with flow visualisation and hot wire anemometry.

6.1. Mean flow development in the channel jet

Velocity profiles were measured with a Pitot tube at the end of the channel and at four downstream positions, $x = 0$, 10, 20, 30, 40 mm, *see* Figure 22. In this figure results from two measurement series are shown. These were taken in the central region of the jet, where the Pitot tube was totally submerged. When this was not the case capillary waves could be seen upstream the point where the surface was disturbed. The occurrence of these waves was determined through visual inspection of the surface of the jet close to the tip of the Pitot tube. Also, if the Pitot tube was not fully inside the jet the measured pressure was slowly fluctuating. This was a result of an unsteady flow past the tip of the tube, *i.e.* the water covered the tube intermittently.

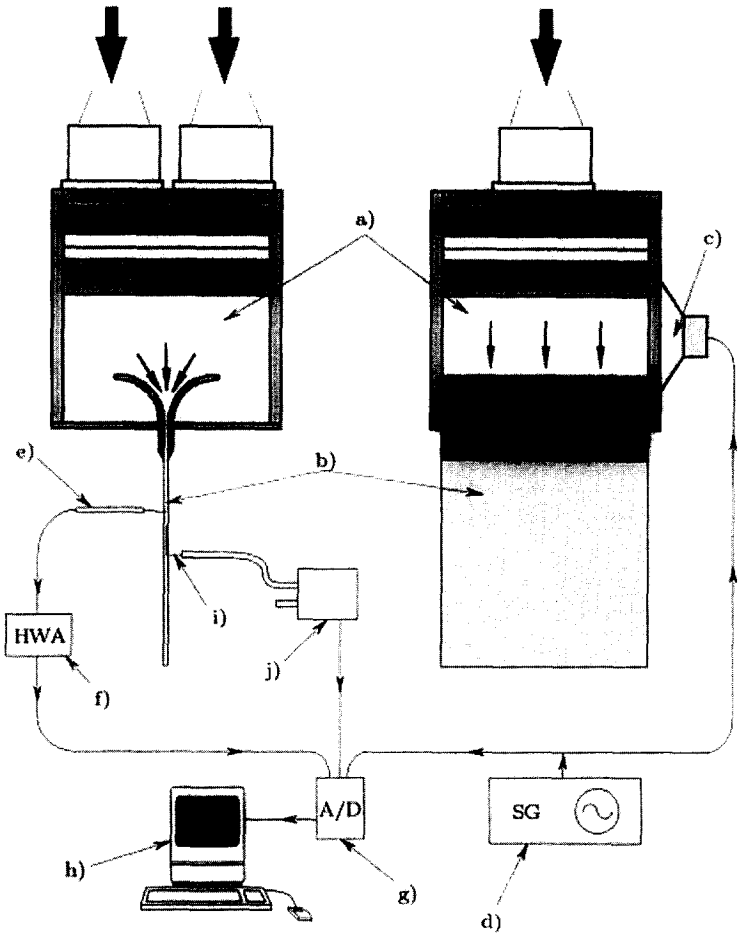

Fig. 21. – Measurements with hot wire anemometry. a) headbox, b) liquid jet, c) loudspeaker, d) signal generator, e) hot wire probe, f) anemometer, g) A/D converter, h) computer, i) pitot tube and j) differential pressure transducer.

The result from a numerical solution, obtained with the method described in chapter 3 of the entrance flow in a plane channel, was fitted to the measured velocity profile at $x = 0$. This gave an entrance length of $\ell_E \approx 80a$, which corresponds well to the length of the plane part of the channel nozzle which is $73a$. The fitted profile at the end of the channel was then used as the upstream boundary condition in a calculation with the same parameters as in the experiment. Since the experimental jet was directed vertically, gravity was included in this calculation.

The result of this calculation can also be seen in Figure 22. As a reference a parabolic profile with the same maximum velocity is also shown. This shows that the flow in the channel was not a fully developed parabolic flow. At the four downstream positions the jet is contracting according to the calculation, as the profile relaxation accelerates the liquid at the surface. The velocity at the centreline of the jet does not decrease, but increases slightly a distance downstream due to gravity.

The region in the jet where measured points satisfy the condition that the Pitot tube should be totally submerged is shrinking downstream, thus implying that the jet is contracting.

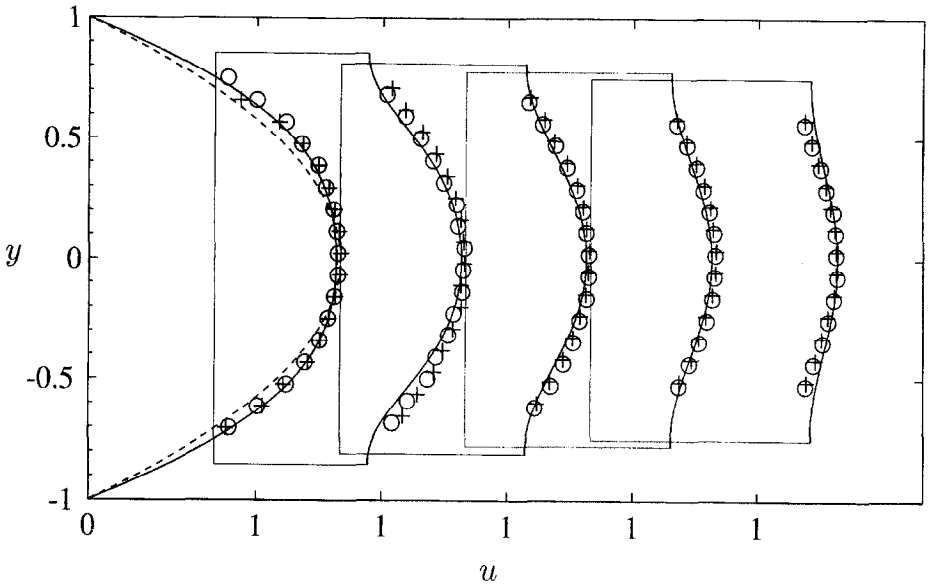

Fig. 22. – Velocity distribution in the channel jet, (—) calculated, (+) and (○) measured, (– –) parabolic profile with the same maximum velocity as the measured profile. $U_m = 1.3$ m/s, $a = 0.55$ mm, $Re = 700$ and $We = 12.5$, profiles at $x = 0$, 10, 20, 30, 40 mm.

6.2. Channel jet instabilities

6.2.1. *Natural waves on the surface of the jet*

The outflow from the plane channel nozzle was visualised with the shadowgraph method, and a series of eight images at different velocities can be seen in Figure 23. The velocities range from 1.3–4.4 m/s and the corresponding Re from 700–2400 and We from 12.5–143. The dark regions at the sides of the jet are the side walls which prevent the spanwise contraction of the jet. Along the sides and at the bottom of the images centimeter markings can be seen. For all images the channel width is 1.1 mm.

At a low velocity, $U_m = 1.3$ m/s, the only disturbance on the jet surface is capillary waves originating from the vertical side walls and free rims at the sides of the jet, Figure 23 *a*. The origins of these capillary waves are primarily the upstream ends of the side walls, which form small upward facing steps to the flow. However, the flow in the centre of the jet is assumed to be unaffected by these disturbances.

When the velocity is increased, $U_m = 1.5$ m/s, periodic darker and brighter lines parallel to the nozzle start to appear in the shadowgraph image, Figure 23 *b*. These are a result of waves on the surface of the jet. The wavelength is of the order of 3 mm.

In Figure 23 *c*, the velocity of the jet is increased further to $U_m = 1.7$ m/s. In the region $x = 7$–8 cm of this image localised irregularities can be seen in the jet, which indicate the development of three dimensional disturbances. These seem to originate from the break-up of the waves and occur randomly.

As the velocity increases the break-up moves closer to the nozzle, Figures 23 *d–f*. The velocities are $U_m = 1.8, 1.9$ and 2.0 m/s, respectively. Also, the location of the break-up becomes more localised to a line parallel with the nozzle when the velocity is increased. Downstream of the break-up, streaky structures in the streamwise direction can be seen in the visualisation, Figures 23 *e,f*. The break-up of the waves cause spray formation on the surface, *i.e.* drops, and at higher velocities the amount of spray increases. In Figures 23 *g,h* it makes the visualisations to become blurry, since the large amount of small drops will deflect the light

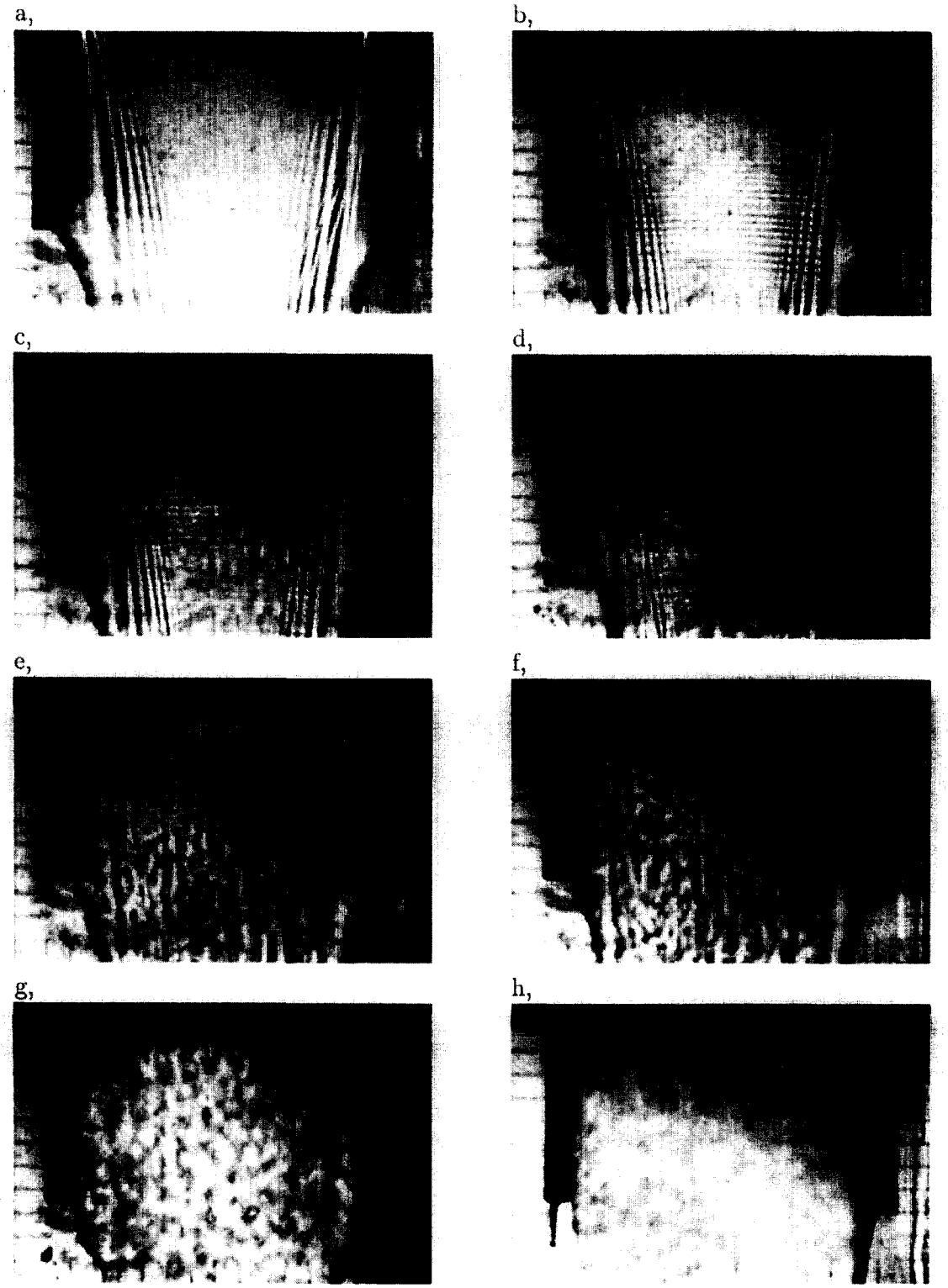

Fig. 23. – Wave development and break-up for naturally occurring disturbances visualised with the shadowgraph technique. a = 0.55 mm, a) 1.3 m/s, b) 1.5 m/s, c) 1.7 m/s, d) 1.8 m/s, e) 1.9 m/s, f) 2.0 m/s, g) 2.2 m/s, h) 4.4 m/s.

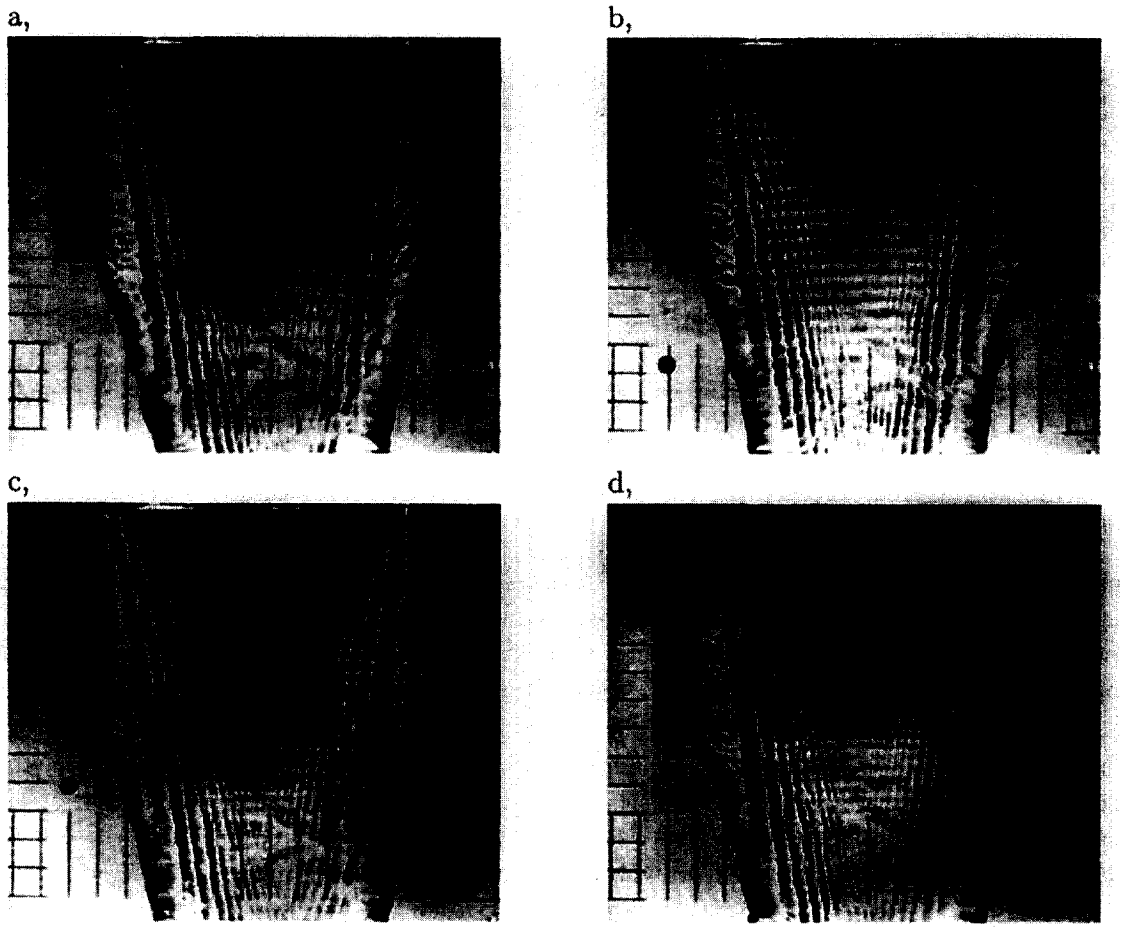

Fig. 24. – Shadowgraph visualisation of forced wave disturbances $Re = 700$, $We = 12.5$ and $a = 0.55$ mm. a) $f = 340$ Hz, b) 485 Hz, c) 612 Hz, d) 669 Hz.

randomly. In the last image the break-up is so strong that holes start to appear in the jet, which can be seen as bright spots in Figure 23 *h*.

6.2.2. *Waves forced by acoustic excitation*

With a loudspeaker attached to the headbox it was possible to trigger waves in the jet at lower Re than for which naturally occurring waves were observed. When this is done with a fixed frequency, the phase of the waves is also fixed, relative to the phase of the loudspeaker signal.

Figure 24 shows a series of four images of the jet at $Re = 700$ at four different forcing frequencies. In the figure the Reynolds number is just below the limit of naturally occurring waves. The images show the response to different frequencies starting at the lowest frequency for which it was possible to obtain waves with the audio equipment used, and ending with the highest frequency. By iteratively lowering the amplitude of the forcing signal and changing the frequency it was possible to determine the frequency for which the waves were most unstable. This frequency was found to be $f \approx 530$ Hz.

By image processing it is possible to get quantitative measurements from these images. Figure 25 *a* shows the variation of the wavenumber α as a function of the distance from the nozzle x, where $x = 0$ corresponds to the outlet of the nozzle. In the graph results for four frequencies are shown and these frequencies are the same

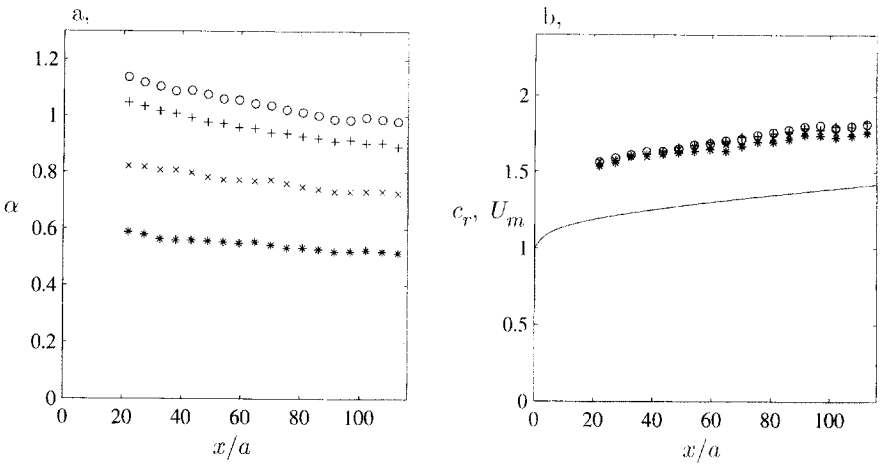

Fig. 25. – The downstream variation of (*a*) the wavenumber and (*b*) phase speed for four frequencies, $Re = 700$, $We = 12.5$ and $a = 0.55$ mm. (∗) $f = 340$ Hz, (×) 485 Hz, (+) 612 Hz, (○) 669 Hz. The calculated mean velocity U_m is indicated by a solid line.

as in Figure 24. As can be seen the wavenumber decreases downstream for all four frequencies, indicating that the phase speed increases. Since the frequencies are known the corresponding phase speeds can be obtained with the aid of the wavenumber variation from Figure 25 *a* as $c_r = \omega/\alpha$. This can be seen in Figure 25 *b*, showing the downstream increase of the phase speed. It is noteworthy that the phase speed evaluated in this way is higher than the mean velocity of the jet.

To facilitate a comparison between linear stability theory and the present experimental results Figure 26 was calculated. This Figure shows curves of constant growth rate for (*a*) the even and (*b*) odd modes, respectively. The contours of constant growth rate are shown as solid black lines and the frequency of the wave disturbance is indicated by white contour lines, labelled with the frequency in Hz. The thick line is the demarcation line between two unstable modes and along this line the frequency change is discontinuous. In the lower two figures (*c*) and (*d*) the growth rate from figures (*a*) and (*b*) have been integrated along lines of constant α.

It is not possible from this graph to explain why the largest sensitivity of the wave disturbance was obtained at $f \approx 530$ Hz, although this frequency is in the range of the most unstable frequencies. It should however be noted that the shutter speed of the camera may play an important role. This since the time integration will damp the contrast and thus the waves will appear as less amplified. It will also shift the observed maxima, e.g. if the shutter speed is 1/2000s, the maximum amplification due to the time integration effect will occur for waves with frequencies $f = (500 + 1000 \cdot N)$ Hz, where $N = 0, 1 \ldots$.

The wavenumber variation in Figure 25 can not be compared directly with the theoretical wavenumber variation along a line with constant frequency, since the image gives information of the spatial variation and the theory is based on a temporal analysis. In order to make an approximate comparison, kinetic wave theory is used (*see* Whitham 1974) where a wave with spatially varying wavenumber is described as

$$w = A\mathrm{e}^{i\Theta(x,t)},$$

where A is the amplitude of the wave and the phase Θ is given by

$$\Theta(x,t) = \alpha(x)x - \omega(\alpha)t.$$

Here $\alpha(x)$ is the local wavenumber, which varies with x. The actual (observed) wavenumber at a streamwise position is then given by

$$\frac{\partial\Theta(x,t)}{\partial x} = \Theta_x = \alpha + x\frac{d\alpha}{dx} - \frac{d\omega}{d\alpha}\frac{d\alpha}{dx}t.$$

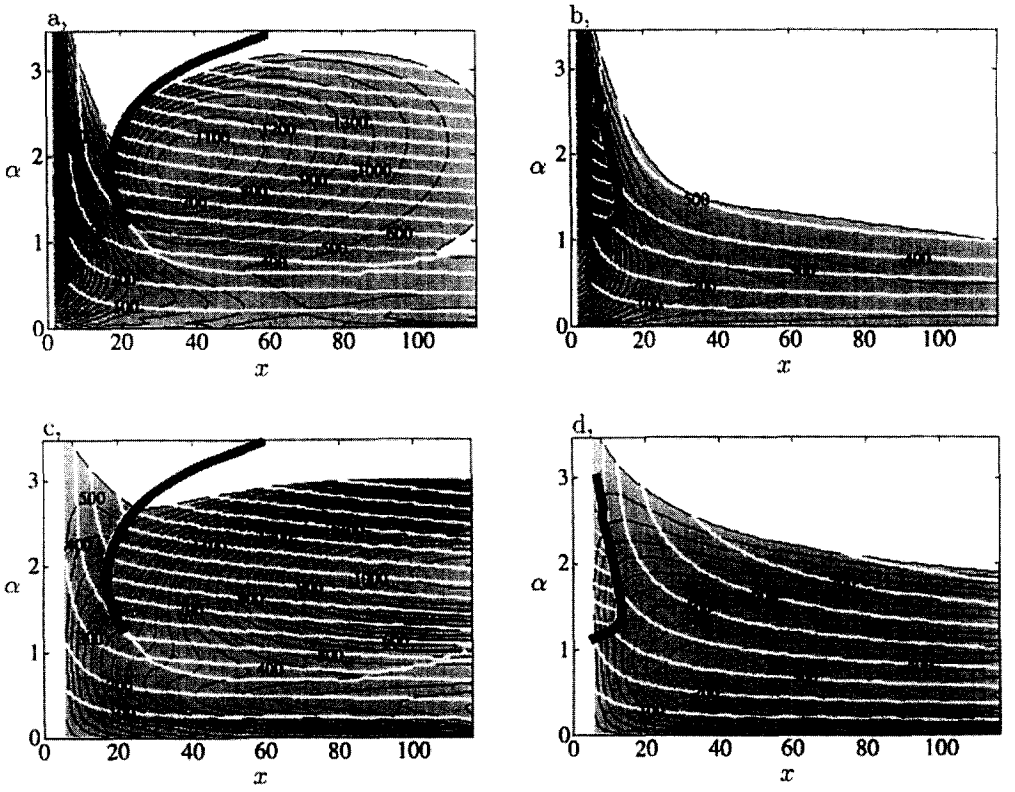

Fig. 26. – Contourplots of the growth rate (top) and integrated growth rate (bottom). The basic flow is calculated with gravity, $Re = 700$, $We = 12.5$ and $Fr = 18$.

But since the frequency is kept constant the last term vanishes and

$$\Theta_x = \alpha + x\frac{d\alpha}{dx}. \tag{42}$$

It is clear that the wavenumber is decreasing downstream and in Figure 27 the measured wavenumber variation from Figure 25 *a* is compared with the theoretical wavenumber variation, both local (obtained directly from Figure 26 *a*) and adjusted according to (42). Hence theory and the experimental results give a similar wavenumber variation, at least qualitatively.

This result also has an effect on the obtained phase speed, which should be given by

$$c_r = \frac{\omega}{\alpha},$$

but in Figure 25, the phase speed was calculated as

$$c_r = \frac{\omega}{\Theta_x}.$$

From Figure 27 it is clear that $\Theta_x \sim 0.75\alpha$, which gives that

$$c_r = \frac{\omega}{\alpha} \approx 0.75\frac{\omega}{\Theta_x}.$$

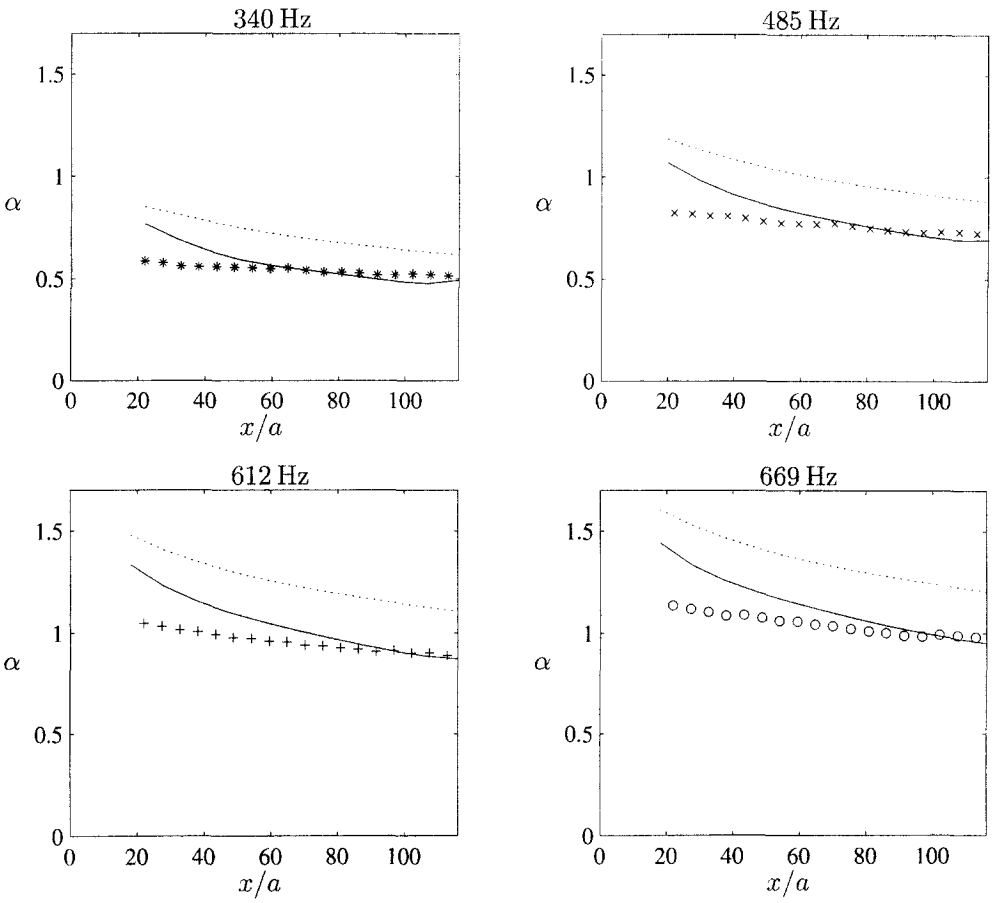

Fig. 27. – The downstream variation of the wavenumber for four frequencies, $Re = 700$ and $We = 12.5$. Dotted lines indicate local wavenumber from theory and solid lines are wavenumber variation after adjustment according to (42).

Hence the true phase speed is lower than in Figure 25 *b*. Actually, with the adjustment (42) the phase speed is close to the mean velocity of the jet, which is also the case for the e_{III} mode.

Since the wave phase is fixed by the signal to the loudspeaker, it is possible to measure the phase difference between this signal and the signal from the hot film anemometer traversed in the normal direction through the jet. The phase- and amplitude distribution in the jet can be seen in Figure 28. The waves are anti-symmetric or sinuous, corresponding to a $\hat{v}$-even mode. In the figure the calculated amplitude distributions for the two most unstable modes (e_{II} and e_{III}) are also shown for the present flow parameters (*i.e.* Reynolds number, velocity distribution and frequency of the disturbance). As can be seen neither of these distributions fit the measured distribution well, however a linear combination of the two give good agreement. At this position only the first mode is unstable, but closer to the inlet the second mode is the most unstable, so therefore both modes may appear simultaneously.

It was also noted that the flow of the surrounding air seems to have little or no influence on the occurrence of these waves. This was investigated by blocking the airflow and changing the geometry outside the jet.

6.2.3. *Break-up of the waves*

The channel jet was also visualised with reflective flakes and a laser sheet in the xz-plane, *see* Figure 20 *ii*. In these visualisations the spanwise homogeneous waves are not visible. However, the break-up of the waves

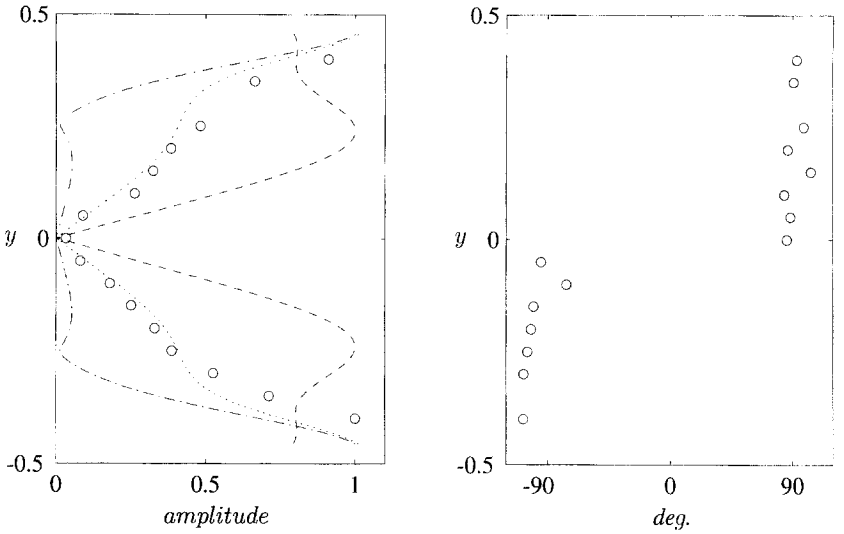

Fig. 28. – Phase distribution in the jet (left) and amplitude distribution (right) in the jet at $x = 40a$. Waves are triggered by a loudspeaker at 530 Hz. $Re = 700$ and $We = 12.5$. The maximum disturbance amplitude is approximately 0.5% of U_m. In the left picture amplitude distributions from linear theory are also shown, (- · -) e_{II} mode, (- - -) e_{III} mode and (· · ·) linear combination.

can be clearly seen, Figure 29. This figure contains images from the visualisation at three different velocities. Both an instantaneous image as well as image-processed and time averaged images are shown. For images a and b $Re = 1030$ and $We = 26.8$, for images c and d $Re = 1090$ and $We = 29.6$ and for images f and g $Re = 1190$ and $We = 35.9$.

At low velocity when the spots start to appear in the shadowgraph visualisation, Figure 23 b, the break-up can be seen as a local phenomenon, Figure 29 a. The break-up originates from a point and it appears to create a pair of streaks originating at this single point. To enhance this structure the image is also shown after performing image-processing with edge-detection, Figure 29 b. The edge-detection routine trace intensity gradients in the image.

At a slightly higher velocity, streaks cover the width of the jet, Figure 29 c. These appear as stronger than the streaks found upstream the break-up. The origins of these streaks are located along a ragged line parallel to the nozzle, and if the break-up is averaged over 100 frames this line can be clearly seen. The break-up line is straight and parallel to the nozzle, Figure 29 d. In the centre of this image the averaging also shows that the break-up occurs more often at specific spanwise locations, which give the streaky structure a clear periodicity. To the left in the averaged image the break-up is more stochastic since the averaging gives a more even reflection from the particles. Upstream of the averaged streaks in the centre of the image low amplitude streaks with the same spanwise location can be seen. These seem to originate from the nozzle.

6.2.4. *Effect of turbulence intensity on the break-up*

To investigate the influence of upstream disturbances on the break-up of the waves the last screen was removed. This gives a higher turbulence level at the entrance of the channel. When the screen was mounted the particles showed a steady laminar flow in the entrance region, and with the screen removed the flow was clearly more turbulent. The break-up of the waves was unaffected by this change at higher velocities when a clear break-up line could be seen in the images, but at low velocities spots could be observed more often with the screen removed, *i.e.* with a relatively higher turbulence intensity. The presence of phase shifts in the waves increased, and also an increase of streaky structures upstream the break-up was found.

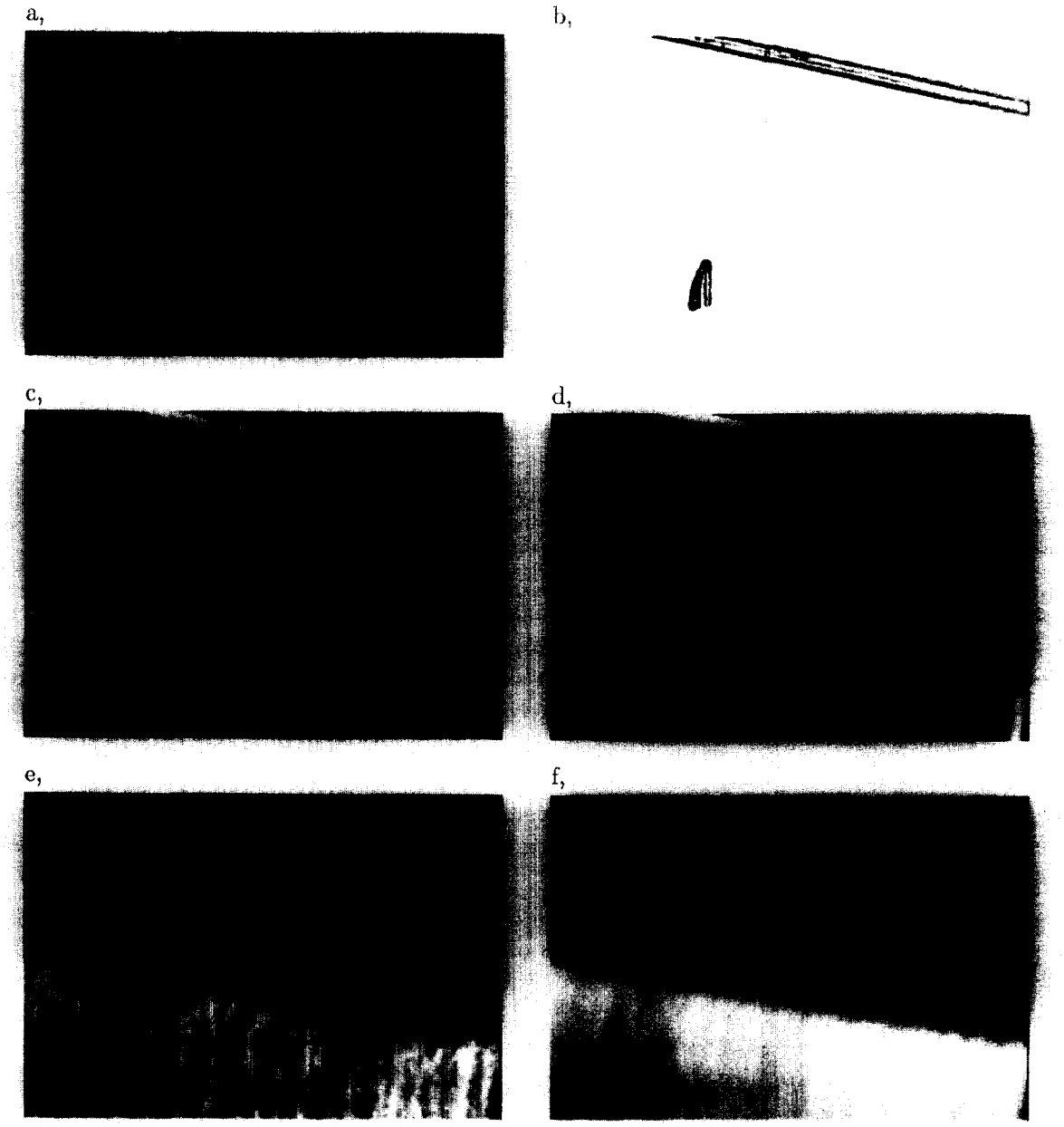

Fig. 29. – Visualisation of the wave break-up with particle visualisation. The straight line at the top is the nozzle outlet, $a = 0.55$ mm. a) and b) localised break-up at $U_m = 1.9$ m/s, c) single frame and d) time average of the break-up at $U_m = 2.0$ m/s, e) single frame and f) time average of the break-up at $U_m = 2.2$ m/s.

6.3. Slit jet

Pitot tube measurements were only performed at one position for the slit nozzle jet, at $x = 20$ mm. The velocity distribution was uniform (within 5%) in the whole region where measurements were possible. As for the channel nozzle, measurements could only be performed when the Pitot tube was completely submerged in the jet.

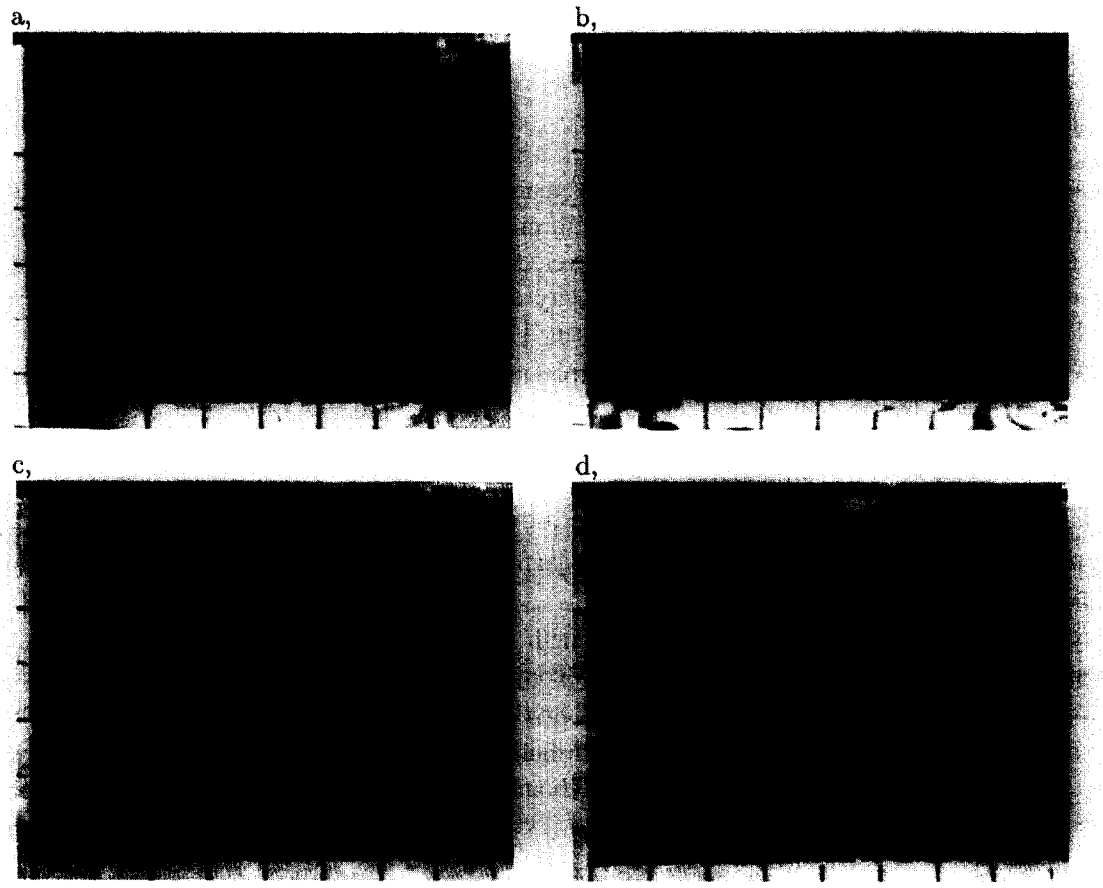

Fig. 30. – Slit jet with particle visualisation, $a = 0.5$ mm. a) $Re = 1300$ and $We = 46$, b) $Re = 2000$ and $We = 110$, c) $Re = 2900$ and $We = 230$, d) $Re = 4000$ and $We = 440$. Scales can be seen at left side and bottom, 1 div.=1cm.

The visualisations were performed by the same methods as for the channel jet. Figure 30 shows 4 images of the slit jet with particle visualisation. The nozzle can be seen at the top of these images, and at the left side and bottom of each of the images a scale with centimeter markings can be seen. The half initial thickness of the jet, $a = 0.5$ mm in all images.

The first of these figures, Figure 30 *a*, show the slit jet at a low velocity, $Re = 1300$. A streaky region in the centre of the jet can be seen, but if compared with the channel jet there is no apparent difference between the two cases. By inspection of the conditions in the nozzle these can be explained in the same way, *i.e.* originating from disturbances inside the nozzle. However, at velocities where waves can be found for the channel jet, the slit jet is undisturbed. Waves could not be found at any velocity, at least not in the range which could be achieved with the present experimental apparatus.

7. Discussion

In order to understand the development of free, plane liquid jets, both the development of the basic laminar flow as well as its stability have been investigated. This includes both the formulation of the problem with the appropriate boundary conditions, obtaining solutions for the basic flow field and to the stability equations for two-dimensional wave disturbances, as well as comparisons with experiments. The experiments have also

shown that the wave instability results in a break-up of the laminar jet. This break-up gives rise to a turbulent jet which appears to contain streaky structures.

7.1. Basic flow development

The basic flow field of the plane liquid jet depends mainly on the nozzle geometry and the Reynolds number. For an inviscid ambient gas the jet will acquire a uniform velocity distribution far downstream. The jet will also contract in the downstream direction. The final jet velocity and width are given by conservation of mass and momentum. The relaxation length, ℓ_R, for the velocity distribution inside the jet was found to be practically independent of how well developed the flow is when it leaves the nozzle.

This seems as first as a paradox but can be explained by the fact that the relevant length scale for the relaxation length will be the half channel width, and therefore it will be independent of the entrance length. When the boundary condition changes at the nozzle outlet and the relaxation process starts momentum has to be re-distributed over the full jet thickness. If instead the re-distribution of the velocity only had to take place over a thin boundary layer close to the jet surface then the entrance length would be an important parameter.

However, for the location of the free surface the relaxation length ℓ_R^h was found to depend on the development length inside the nozzle.

A fully developed flow will give a relaxation length for the jet thickness which is about one-fifth of the relaxation length for the velocity distribution to become uniform. It was also found that the characteristic downstream development lengths ℓ_R and ℓ_E are proportional to Re.

A viscous ambient gas will affect the velocity distribution in the jet slightly. Here a thin boundary layer will develop at the surface of the jet in order to fulfil the boundary condition of no-slip. The relaxation process will be slowed down and further downstream it will also give an expansion of the jet, in contrast to the case with an inviscid outer gas. This expansion takes place since momentum flux is drained from the liquid jet to the ambient gas by the shear on the surface. In all physical applications a viscous gas will be present, and because of this the jet will never become uniform far downstream. Instead it will continue to expand. However, if the viscosity and density of the gas are lower than for the liquid this process can be considered to be slow.

The inviscid flow from the slit nozzle was calculated by (Söderberg, 1994). Both these results and the present measurements clearly show that the basic flow is well described by inviscid theory. For this case boundary layers will of course be present because of the no-slip condition at the nozzle walls, but these will be very thin at the exit since the flow is strongly accelerated. For nozzles with contraction angles that are in between the channel and slit nozzles (*i.e.* in between 0 and 90 degrees) there will be a gradual change from fully developed viscous flow to an almost inviscid flow.

7.2. Instabilities and break-up of plane liquid jets

Laminar shear flows which have a velocity distribution with an inflection point, where the shear is at a maximum, are known to be highly unstable. This is, according to linear stability theory for parallel flows a necessary but not sufficient condition for the jet to be inviscidly unstable, *see* e.g. (Drazin and Reid, 1981). In the case of a channel flow nozzle the relaxation of the jet velocity distribution from parabolic-like at the channel outlet to uniform, results in a velocity distribution with inflection points close to the jet surfaces. These may give rise to inflection type wave instabilities. In the experiments with the channel flow nozzle wave disturbances were observed to occur naturally.

The stability calculations were made assuming two-dimensional wave disturbances. Furthermore the flow was assumed to be locally parallel, *i.e.* the wave length of the wave disturbance was assumed to be small compared

to the characteristic length scale for the development of the basic flow field. The stability was investigated in the temporal sense where the stability of a disturbance of a specific wave length is considered. Two types of wave disturbances may exist, either sinuous or dilatational. Depending on the parameters of the problem (such as the Reynolds number and the basic velocity distribution) one or several modes may be unstable. For typical parameter ranges studied up to five different unstable modes were found. Three of these were sinuous (anti-symmetric) and two were dilatational (symmetric). The two symmetric modes have counterparts in the anti-symmetric modes and the first of these two pairs has eigenfunctions with a maximum amplitude at the point of inflection. The other pair of modes has its maximum growth located at low wavenumbers. These two modes have their maximum amplitude at the surface.

Modes *I* and *II* are identical to the modes found by (Hashimoto and Suzuki, 1991). Mode *I* is what they called a soft-mode instability and mode *II* is the so called hard-mode. Their calculations were based on velocity profiles calculated with an approximate method, (Lienhard, 1968). This method gives a weaker relaxation of the velocity profiles and hence overpredicts the relaxation length. They did not include an ambient gas in their calculation. The comparison they made between experiments showed a fair agreement with the stability calculations, when the observed wavenumber variation in the streamwise direction was compared with the location of maximum growth, α, for mode *I*. However, their calculation, with which they compare the experimental results, does not include surface tension and they later show that surface tension has a considerable effect on both growth rate and phase speed. The flow is spatially varying and the disturbance should be frequency locked in this flow situation (*i.e.* the frequency should be constant). Hence wavenumber variation will not follow the maximum growth ridge in the plane given by the parameters α and x/Re.

Both modes *I* and *II* exist without an ambient gas, which is obvious since (Hashimoto and Suzuki, 1991) did not include an ambient gas in their calculations. Hence they are not identical to any of the modes found by (Hagerty, 1955), (Lin *et al.*, 1990) or (Li and Tankin, 1991). As can be seen from the calculations with a uniform velocity distribution, Figure 16, the jet is unstable for higher Reynolds numbers. Due to the 'valley' in the lower part of the contourplots near $Re = 1000$ it is possible that there could be a change in instability mechanism at this location. Also, a decreased shear on the surface (increased boundary layer thickness), reduces the instability. This can be seen from that the growth rate decreases for positions further downstream.

Mode *I* only occurs when the relaxing profile is present and it has its highest growth rate for the early profiles, *i.e.* close to the nozzle. In Figure 14 it is obvious that this mode becomes unstable when the Reynolds number is increased. Also, the growth rate seems to be independent of high Reynolds numbers. This implies that viscosity does not play an important role for higher Reynolds numbers and that the instability thus is 'inviscid'.

The fifth mode (e_{III}), is only found in a limited part of the parameter space. The eigenfunction of $\hat{v}$ shows that the amplitude is zero at the surface for low Re. This means that it does not distort the jet surface and can therefore not be observed through shadowgraph visualisation. The origin of this mode is not clear but its boundedness in Reynolds number should imply that it is a 'viscous' instability. Since it also requires a velocity profile it is not the viscosity enhanced instability found by (Li and Tankin, 1991).

The measured amplitude distribution of the forced wave disturbance was found to originate from a sinuous mode. However, neither of the three modes could approximate the amplitude distribution accurately. Instead a linear combination of the surface wave mode (e_{II}) and the fifth mode (e_{III}) gives a good approximation of the measured distribution.

The break-up of the waves creates strong streaky structures in the jet which are stronger than the streaks originating from the nozzle. This can be judged based on the appearance of the streaks with particle visualisation. The origin of the break-up is not clear, but may be related to the interaction between two or more unstable modes. It could also be the presence of an absolute instability that causes this localised break-up.

7.3. Conclusions

If a plane liquid jet emanates from a nozzle with a partially or fully developed flow the process of velocity profile relaxation will always be present. The effect of this process depends on the contraction ratio of the nozzle. A slit nozzle will give a velocity distribution which is close to that of the potential flow solution.

The profile relaxation process may cause a wavy instability of the jet. Linear stability theory as well as experiments have shown that the most unstable mode is of sinuous type, which was also shown by (Hashimoto and Suzuki, 1991). Controlled experiments where a wave disturbance was excited at the nozzle show how the wave number and frequency of the disturbance are related. This also gives that the phase speed of the waves is close to the mean flow speed of the jet.

The waves found in the experiments could not be explained by the theoretical results obtained by (Hagerty and Shea, 1955), (Lin *et al.*, 1990) or (Li and Tankin, 1991). They were also compared to the four instability modes found theoretically by (Hashimoto and Suzuki, 1991). However, also these modes seemed to be inadequate to explain the observed waves and measured amplitude distribution within the jet.

A new mode was found which only was present as a sinuous wave. Agreement was found between the experimental disturbance amplitude distribution and a linear combination of this new mode and one of the modes found by (Hashimoto and Suzuki, 1991). The observed phase speed also showed a fair agreement with the phase speed predicted by linear theory.

The instability waves were found to increase in amplitude in the downstream direction and break up if the velocity of the liquid is high enough. The break-up results in strong streamwise streaks which affects the whole width of the jet. It will also cause partial disintegration of the jet, *i.e.* spray formation. The streamwise streaks caused by the break-up is much stronger than streaks originating from the inside of the nozzle.

In order to fully understand the importance of the different modes it is believed that investigations should be undertaken which include effects of a non-parallel flow and the possibility for absolute instability. This could possibly explain the break-up of the waves. Also, the influence of up-stream conditions, e.g. turbulence level or localised disturbances, in the headbox should also be investigated experimentally.

Acknowledgements. – This work has been funded by NUTEK, the Swedish National Board for Industrial and Technical Development.

REFERENCES

Batchelor G. K., 1967, *An Introduction to Fluid Dynamics*, Cambridge University Press.

Brennen C., 1970, Cavity surface wave patterns and general appearance., *J. Fluid Mech.*, **44**, 33.

Bogy D. B., 1979, Drop Formation in a Circular Liquid Jet., *Ann. Rev. Fluid Mech.*, **11**, 207–227.

Chandrasekhar S., 1961, *Hydrodynamic and Hydromagnetic Stability*. Oxford: Clarendon Press.

Debler W., Yu D., 1988, The Break-up of Laminar Liquid Jets., *Proc. Roy. Soc. Lond. A*, **415**, 106–120.

Drazin P. G., Reid W. H., 1981, *Hydrodynamic Stability*. Cambridge University Press.

Gavis J., Modan M., 1967, Expansion and contraction of jets of Newtonian liquids in air: Effect of tube length., *Phys. Fluids*, **10**, 487–498.

Goedde E. F., Yuen M. C., 1970, Experiments on liquid jet instability., *J. Fluid Mech.*, **40**, 495–514.

Hagerty W. W., Shea J. F., 1955, A Study of the Stability of Plane Fluid Sheets., *J. Appl. Mech.* **22**, 509–514.

Hashimoto H., Suzuki T., 1991, Experimental and Theoretical Study of Fine Interfacial Waves on Thin Liquid Sheet., *JSME Int. J. Series II*, **34**, No. 3, 277–283.

Hoyt J. W., Taylor J. J., 1968, Waves on water jets., *J. Fluid Mech.*, **83**, 119–227.

Joseph D. D. 1978, Slow Motion and Viscometric Motion; Stability and Bifurcation of the Rest State of a simple Fluid., *Arch. Rat. Mech. Anal.*, **56**.

Lamb H., 1932, *Hydrodynamics*, 6th edn. Dover.

Leib S. J., Goldstein M. E., 1986, The generation of capillary instabilities in a liquid jet., *J. Fluid Mech.*, **168**, 479–500.

LI X., TANKIN R. R., 1991, On the temporal stability of a two-dimensional viscous liquid sheet., *J. Fluid Mech.*, **226**, 425–443.
LIN S. P., LIAN Z. W., CREIGHTON B. J., 1990, Absolute and convective instability of a liquid sheet., *J. Fluid Mech.*, **220**, 673–689.
LIENHARD J. H., 1968, Effects of Gravity and Surface Tension Upon Liquid Jets Leaving Poiseuille Tubes., *J. Basic Eng.*, **226**, 425–443.
LUCA L., COSTA M., 1997, Instability of a spatially developing sheet., *J. Fluid Mech.*, **331**, 127–144.
MANSOUR A., CHIGIER N., 1995, Dynamic behaviour of liquid sheets., *Phys. Fluids A*, **3**, 2971–2979.
MIDDLEMAN S., GAVIS J., 1995, Expansion and Contraction of Capillary Jets of Newtonian Liquids., *Phys. Fluids*, **4**, 355–360.
MACCARTHY M. J., MOLLOY N. A., 1974, Review of Stability of Liquid Jets and the Influence of Nozzle Design., *Chem. Engng. J.*, **7**, 1–20.
NICKELL R. E., TANNER R.I., CASWELL B., 1968, The solution of viscous incompressible and free surface flows using finite element methods., *J. Fluid Mech.*, **65**, 189–206.
NORMAN B., 1996, Hydrodynamic developments in twin-wire forming – An overview., *Paperi ja Puu – Paper and Timber*, **78**, (6–7), 189–206.
PAI S. I., 1954, *Fluid Dynamics of Jets.* Van Nostrand.
PLATEAU J., 1873, Statique expérimentale et théorique des liquides soumis aux seules forces moléculaires, cited by Lord Rayleigh in *Theory of Sound*, 2nd edn, vol. II. Dover.
RAYLEIGH Lord. 1896, *Theory of Sound*, 2nd edn, vol. II. Dover.
SAVART F. 1833, *Ann. Chem.*, **53**, 337.
SCHLICHTING H., *Boundary layer theory*, 7th edn. McGraw-Hill .
SÖDERBERG D., 1994, *An Experimental Study of the Stability of Plane Liquid Jets.* M.Sc.Thesis, Dept. of Mechanics, Royal Institute of Technology. Reprint, TRITA-MEK TR 1996:5.
TAYLOR G. I., 1959, The dynamics of thin sheets of fluid III. Disintegration of fluid sheets., *Proc. Roy. Soc. A*, **253**, 313–321.
TENG C. H., LIN S. P., CHEN J. N., 1997, Absolute and convective instability of a viscous liquid curtain in a viscous gas., *J. Fluid Mech.*, **332**, 105–120.
TILLET J. P., 1968, On the laminar flow in a free jet of liquid at high Reynolds numbers., *J. Fluid Mech.*, **32**, 273–292.
VAN DYKE M., 1970, Entry flow in a channel., *J. Fluid Mech.*, **44**, 813–823.
WEINSTEIN S. J., CLARKE A., MOON A. G., SIMISTER E. A., 1997, Time-dependent equations governing the shape of a two-dimensional liquid curtain, Part 1: Theory., *Phys. Fluids*, **9**, 3625–3636.
YAKUBENKO P. A., 1997, Capillary instability of an ideal jet of large but finite length., *Eur. J. Mech. B/Fluids.*, **16** (1), 39–47.
YU T., LIU T., 1992, Numerical solution of a Newtonian jet emanating from a converging channel., *Computers Fluids*, **21**, No. 4, 813–823.
WOLF D. H., INCROPERA F. R., WISKANTA R., 1995 Measurement of the turbulent flowfield in the free-surface jet of water., *Exp. in Fluids*, **18**, 397–408.

(Received 10 September 1997,
revised 26 March 1998,
accepted 27 January 1998)